

1 **Isotopic Fractionation Accompanying CO₂ Hydroxylation and**
2 **Carbonate Precipitation from High pH Waters at The Cedars,**
3 **California, USA**

4 John N. Christensen^{1*}, James M. Watkins², Laurent S. Devriendt³, Donald J. DePaolo^{1,4},
5 Mark E. Conrad¹, Marco Voltolini¹, Wenbo Yang⁵, and Wenming Dong¹

6 ¹Earth and Environmental Science Area, Energy Geosciences Division, Lawrence
7 Berkeley National Laboratory, Berkeley, CA 94720.

8 ²Department of Earth Sciences, University of Oregon, Eugene, OR 97403

9 ³Royal Netherlands Institute for Sea Research (NIOZ), Landsdiep 4, 1797 SZ 't
10 Horntje, The Netherlands

11 ⁴Department of Earth and Planetary Science, University of California, Berkeley, CA
12 94720.

13 ⁵Department of Integrative Biology, University of California, Berkeley, CA 94720.

14 *Corresponding author jchristensen@lbl.gov

15 **Abstract**

16 The Cedars ultramafic block hosts alkaline springs (pH > 11) in which calcium
17 carbonate forms upon uptake of atmospheric CO₂ and at times via mixing with
18 surface water. These processes lead to distinct carbonate morphologies with “flocs”
19 forming at the atmosphere-water interface, “snow” of fine particles accumulating at
20 the bottom of pools and terraced constructions of travertine. Floe material is mainly
21 composed of aragonite needles despite CaCO₃ precipitation occurring in waters with
22 low Mg/Ca (<0.01). Precipitation of aragonite is likely promoted by the high pH
23 (11.5-12.0) of pool waters, in agreement with published experiments illustrating the
24 effect of pH on Ca-carbonate polymorph selection.

25 The Ca-carbonates exhibit an extreme range and approximately 1:1 covariation
26 in δ¹³C (−9 to −28‰ VPDB) and δ¹⁸O (0 to −20‰ VPDB) that is characteristic of
27 travertine formed in high pH waters. The large isotopic fractionations have
28 previously been attributed to kinetic isotope effects accompanying CO₂
29 hydroxylation but the controls on the δ¹³C-δ¹⁸O endmembers and slope have not
30 been fully resolved, limiting the use of travertine as a paleoenvironmental archive.
31 The limited areal extent of the springs at The Cedars (~0.5 km²) and the limited
32 water sources, isotopic compositions and temperatures, combined with our
33 sampling strategy and the addition of Ca isotopic measurement, allow us to place
34 tighter constraints on the processes involved in generating the systematic C and O
35 isotope variations.

36 We develop an isotopic reaction-diffusion model and an isotopic box model for a
37 CO₂-fed solution that tracks the non-equilibrium isotopic composition of each
38 dissolved inorganic carbon (DIC) species and CaCO₃. The box model includes four
39 sources or sinks of DIC (atmospheric CO₂, high pH spring water, fresh creek water,

53 HCO_3^- , pH = 7.8-8.7) that occasionally or locally mixes with the high-
54 pH spring water. The bulk carbonate $\delta^{13}\text{C}$ and $\delta^{18}\text{O}$ values of modern and ancient
55 travertines therefore reflect the proportion of calcium carbonate formed by
56 processes (1) and (2), with process (2) dominating the carbonate precipitation
57 budget at The Cedars. These results show that recent advances in understanding
58 kinetic isotope effects allow us to model complicated, but common natural
59 processes, and suggest ancient travertine may be used to retrieve past surface water
60 $\delta^{18}\text{O}$ and atmospheric $\delta^{13}\text{C}$ values. There is evidence that older travertine at The
61 Cedars records atmospheric $\delta^{13}\text{C}$ that predates large-scale combustion of fossil fuels.

62 **1. Introduction**

63 Most Earth-surface carbonate minerals precipitate out of stable isotopic
64 equilibrium with their host aqueous solution (Coplen, 2007; Watkins et al., 2013,
65 2014; Devriendt et al., 2017; Daëron et al., 2019). Deviations from equilibrium are
66 manifested in a variety of ways. One of the most striking ways, still not fully
67 understood, is a strong correlation between $\delta^{13}\text{C}$ and $\delta^{18}\text{O}$ in carbonates
68 precipitated under different circumstances, from marine calcifying organisms (e.g.,
69 McConnaughey, 1989; Spero et al., 1997; Adkins et al., 2003; Kimball et al., 2014;
70 Hermoso et al., 2014; Chen et al., 2018), to cryogenic calcium carbonates (Clark and
71 Lauriol, 1992; Žák et al., 2008), lacustrine carbonates (Talbot, 1990), and
72 speleothem carbonates formed by CO_2 degassing (Daëron et al., 2011; Tremaine et
73 al., 2011). The slope of the $\delta^{13}\text{C}$ - $\delta^{18}\text{O}$ co-variation varies from place to place because

74 each setting is somewhat unique and because kinetic isotope effects in the DIC-H₂O-
75 CaCO₃ system are sensitive to factors such as temperature, solution pH, mixing
76 between DIC reservoirs, the residence time of DIC in solution, whether CO₂ is
77 ingassing or outgassing from solution, and whether the system is open versus closed
78 (e.g. McConaughy, 1989; Clark et al., 1992; Falk et al., 2016; Devriendt et al., 2017;
79 Chen et al., 2018).

80 Ca-carbonates formed in hyperalkaline springs exhibit some of the largest
81 and most systematic variations of $\delta^{13}\text{C}$ and $\delta^{18}\text{O}$ (O'Neil and Barnes, 1971; Clark and
82 Fontes, 1990; Clark et al., 1992; Meister et al., 2011; Leleu et al., 2016; Falk et al.,
83 2016). The archetype locality is a set of carbonate formations precipitating from
84 springs emanating from serpentized peridotite in the Samail ophiolite, Sultanate
85 of Oman (Barnes et al., 1978; Clark et al., 1992; Kelemen et al., 2011; Mervine et al.,
86 2014; Falk et al., 2016). Figure 1 (data from Falk et al., 2016; Mervine et al., 2014;
87 Clark et al., 1992; Clark and Fontes, 1990) shows the strong $\delta^{13}\text{C}$ - $\delta^{18}\text{O}$ correlation
88 spanning a range of about 25‰, with most of the values being isotopically lighter
89 than the expected equilibrium value. The isotopically light endmember of the $\delta^{13}\text{C}$ -
90 $\delta^{18}\text{O}$ array has been attributed to hydroxylation of dissolved CO₂ ingassing from the
91 atmosphere (Clark et al., 1992). The rest of the array has been attributed to some
92 combination of mixing between different DIC sources, partial equilibration of DIC,
93 and post-depositional recrystallization (Falk et al., 2016). Recent progress has been
94 made on the development of numerical models that quantify kinetic isotope effects
95 in the DIC-H₂O-CaCO₃ system (Devriendt et al., 2017; Sade and Halevy, 2017; Chen
96 et al., 2018), providing an opportunity to gain a more quantitative understanding of
97 the peculiar and large kinetic isotope effects in high pH environments.

98 The Ca-carbonate samples from Oman represented in Fig. 1 were collected
99 over an area of 50 km x 200 km from calcium-hydroxide springs (pH = 11.2-12.1)
100 spanning a large range in temperature (22-32°C), possibly large range in $\delta^{13}\text{C}$ of DIC
101 surface and ground waters, and large range in the age of samples (0 to 40 ka). This is
102 the main reason the range of possible equilibrium calcite values is large (Fig. 1). In
103 this study, we investigate a similar high-pH system, The Cedars, where the springs

104 are within a 0.5 km² area, and the spring waters have a more constant temperature
105 (17.4 ± 1°C) and δ¹³C composition. Recognizing that kinetic isotope effects are
106 growth-rate-dependent, our approach is to determine the calcite and aragonite
107 growth rates using Ca isotopes and detailed field observations, and produce a
108 dataset where the δ¹³C and δ¹⁸O values of the minerals could be evaluated in the
109 context of these growth-rate data and with reference to the growth conditions,
110 travertine forms, and likely controls on CO₂ transport.

111 **2. The Cedars**

112 The Cedars (aka Cazadero e.g. Barnes et al. 1967) peridotite is a relatively small
113 tectonically emplaced fault-bounded wedge of ultramafic rock located in the
114 California Coast Range north of San Francisco (Blake et al 2012, Coleman 2000) (Fig.
115 2). The dominant rock type is harzburgite with lesser amounts of dunite. This
116 fragment of Jurassic age oceanic lithosphere has been inferred to be an obducted
117 abyssal peridotite from an oceanic fracture zone (Coleman 2000), or alternatively as
118 the basal peridotite of the Coast Range Ophiolite formed in the mantle wedge above
119 the Mesozoic California-margin subduction zone (Choi et al. 2008). The central
120 portion of The Cedars is partially serpentinized, while the margins consist of
121 sheared serpentinite (Blake et al. 2012). The Cedars ultramafic body is in fault
122 contact with Franciscan Complex mélangé greywacke and shale (Coleman 2000). It
123 has a dipping, wedge-shaped structural geometry, extending to a depth of 4km but
124 with an average thickness of only 2km or less (Blake et al. 2002).

125 A series of springs emerge along the course of Austin Creek at the bottom of the
126 main canyon between ~275 m and 335 m elevation. Some springs produce pools
127 and terraced deposits adjacent to the creek before emptying into the creek. At other
128 locations springs enter the creek directly from the bottom. An example at the
129 Barnes Spring Complex (BSC, Fig. 2) of a spring-fed pool adjacent to Austin Creek is
130 shown in Fig. 3. The unusual nature of the springs at The Cedars was first
131 recognized and described by Barnes et al. (1967). They found that the springs
132 produce low-temperature (~18 °C) ultrabasic waters with high pH (11.7), nil
133 carbonate, low Mg, Fe, and silica concentrations but relatively high Ca. They

134 attribute the spring water's unusual chemical characteristics to involvement in on-
135 going serpentinization of primary ultramafic rock at shallow depth (see also Barnes
136 and O'Neil, 1969). A subsequent stable isotopic study demonstrated that the spring
137 waters have a meteoric origin as opposed to an ancient connate origin from the
138 underlying Franciscan formation (Barnes and O'Neil, 1969; Barnes et al. 1978), and
139 that Ca-carbonates precipitating from the ultrabasic waters have unusually low $\delta^{13}\text{C}$
140 and $\delta^{18}\text{O}$ values (O'Neil and Barnes, 1971).

141 Morrill et al. (2013) conducted a more extensive study of the high pH waters of
142 The Cedars. They identified two types of ultrabasic water at The Cedars that
143 variably mix: (1) waters with deep flow-paths that interacted with the underlying
144 Franciscan Complex enriching the waters in K^+ , salinity, and volatile organic
145 compounds before encountering ultramafic rock, and (2) waters with shallow paths
146 that pass solely through ultramafic rock and are characterized by lower salinity and
147 $[\text{K}^+]$. The springs exhibit stable temperatures with time and season (spring vs. fall),
148 averaging about $17 \pm 1^\circ\text{C}$ (Morrill et al., 2013; Suzuki et al., 2013). Tritium dating of
149 water samples by Suzuki et al. (2017) indicates that water with deep flow paths, as
150 at the Grotto Pool Springs, has an age greater than 60 years (<0.8 Tritium units, TU),
151 while Barnes Complex spring water, with an inferred shallow flow path, gave a value
152 of 2.3 TU, possibly indicating an age younger than 10 years since that value is
153 similar to contemporaneous Bay Area precipitation (1.3-2.2 TU; Harms 2015).

154 **3. Methods**

155 **3.1 Sampling**

156 Samples for this study were collected on eight visits to The Cedars in 2013, 2014,
157 2016, and 2018. Four sites were sampled (Fig. 2): (1) The Wedding Cake above
158 Mineral Falls, (2) The Barnes Spring Complex (BSC), (3) Grotto Pool Springs (GPS),
159 and (4) "New" Pool within Austin Creek ~ 250m upstream of BSC. Water samples
160 from the high pH springs and from Austin Creek were filtered to $0.22 \mu\text{m}$ using
161 Durapore filter units (Millipore), collected in HDPE bottles and acidified to pH 2
162 using high purity HNO_3 (Baseline Nitric Acid, Seastar Chemicals). Prior to collection,
163 the pH of the sampling source was measured with an Orion hand-held pH meter

164 (Thermo Scientific). Samples of Ca-carbonate collected are of several types as
165 illustrated in Fig. 3: (1) partially consolidated material from rims of pools (e.g.
166 Wedding Cake); (2) precipitates from the surfaces of pools (called here floes); (3)
167 dendritic forms and encrustations from sites of creek-spring mixing; (4)
168 unconsolidated material (called here snow) from pool bottoms; and (5) solid, old
169 travertine deposits (sample collected at BSC). Surface floes were either skimmed
170 from the surface or captured on screens.

171 **3.2 Analytical Methods**

172 Below are given brief descriptions of the analytical techniques used in this study.
173 Further details are provided in the Supplement.

174 Samples of Ca carbonate and water were analyzed for Ca isotopic composition
175 using thermal ionization mass spectrometry on a Triton (mfd. by ThermoFisher)
176 multicollector instrument. Prior to chemical separation, samples were spiked with a
177 double ^{42}Ca - ^{48}Ca double spike. The Ca isotope results are reported as per mil
178 deviations of the $^{44}\text{Ca}/^{40}\text{Ca}$ ratio ($\delta^{44}\text{Ca}$) from Bulk Silicate Earth (BSE) (Nielsen et al.
179 2011). We have confirmed with recent measurements that our BSE reference
180 $^{44}\text{Ca}/^{40}\text{Ca}$ ratio is $0.96 \pm 0.05\%$ higher than the value for SRM915a.

181 Oxygen and carbon isotopic analyses of carbonate samples were conducted in
182 the Center for Stable Isotope Biogeochemistry (CSIB), Department of Integrative
183 Biology, University of California, Berkeley, using a GV IsoPrime mass spectrometer
184 equipped with Dual-Inlet and MultiCarb systems. Results are reported relative to
185 VPDB (Vienna Pee Dee Belemnite). The overall external analytical precision is \pm
186 0.05% for $\delta^{13}\text{C}$ and $\pm 0.07\%$ for $\delta^{18}\text{O}$.

187 Elemental compositions (metal concentrations) of the water samples were
188 determined by Quadrupole-ICPMS (Elan DRC II, PerkinElmer SCIEX, USA). Images of
189 Ca-carbonate samples were obtained with a Zeiss EVO-LS10[®] microscope, with
190 capabilities of secondary electrons (SE) imaging and back-scattered electrons (BSE)
191 imaging. Phase identification and quantification in selected solid samples were
192 carried out via X-Ray powder diffraction with a Rigaku SmartLab[®] X-ray
193 diffractometer.

194 **4. Results**

195 **4.1 XRPD and SEM observations**

196 Fourteen carbonate samples were selected for powder XRPD analysis to cover
197 the observed range in sample texture. The fractions of the identified mineral phases
198 are given in Table 1. Material from pool edges ranges from 99.7% aragonite
199 (Wedding Cake) to 46.6% aragonite (BSC Pool B). Aragonite and/or calcite are
200 found in all samples, with aragonite ranging from 18% to 99.7%, and calcite ranging
201 from 0.14% to 82%. Small amounts of vaterite (a polymorph of Ca carbonate) were
202 identified in one floe sample (BSC Carb I, $0.5 \pm 0.2\%$) and in one sample of a pool
203 edge (BSC PE-C2 "crust" $0.6 \pm 0.2\%$). Brucite ($\text{Mg}(\text{OH})_2$) was found in some samples
204 of BSC pool edges (PB-C2, PE-C2 3 and 8%, respectively) in a filtered snow sample
205 from BSC (PB-1 6.8%), from a GPS pool (Carb K 0.5%), and in one of the samples
206 from mixed spring-creek water (Carb AA 7.7%). In samples of snow filtered from
207 GPS pool water both hydromagnesite (Carb J 27%; Carb K 49.5%) and
208 nitromagnesite (Carb J 4.5%; Carb K 2.3%) are detected. Nesquehonite
209 ($\text{MgCO}_3 \cdot 3\text{H}_2\text{O}$) was also detected in one sample (3% in Carb K).

210 The sample of the rim of the Wedding Cake (Carb A) was at collection relatively
211 firm, yet still friable. The SEM images of the material (Fig. S1) show elongate crystals
212 up to 10-15 μm of aragonite (as identified by the XRPD analysis) gathered in
213 bundles, sprays and spheres. The samples from the New Pool (Carb B and Carb C)
214 affected by creek mixing, is also identified by XRPD as 100% aragonite, and consist
215 of sharp needles of aragonite up to at least 40 μm grouped in radial sprays or
216 spheres (Fig.s S2 and S3). Both the soft encrustation on rock and the elongate
217 branching forms display similar micro-textures.

218 The samples of floes have a more varied mineralogy and texture than samples
219 from the Wedding Cake and from the New Pool. Figure 4 compares the inferred top
220 (upwards from water) and bottom (down into the water) surfaces of floe Ca-
221 carbonates from a BSC pool. The inferred top-side of the floe (Fig. 4A) displays
222 radiating horizontal sprays of aragonite crystals, forming a relatively flat surface. In
223 contrast, the inferred bottom side (Fig. 4B) is rougher, with the terminations of the

224 aragonite sprays forming a hummocky surface. Calcite rhombohedra are scattered
225 across this surface, apparently forming largely after growth of the aragonite sprays.
226 Open areas constitute approximately 15-20% of the area of this floe sample (Carb.
227 D). Fig. S4 in the Supplement provides views of the broken edges of this floe
228 material (Carb D). In the cross-sections the aragonite sprays can be seen to radiate
229 from points, forming intersecting hemispheres. In this case the floe has a thickness
230 of about 10 to 12 μm . Similar differences between the tops and bottoms of floes are
231 confirmed by examination of carefully collected samples so that flakes of known
232 original orientation could be examined by SEM (Fig. 4C).

233 The growth rate of the floes was determined by measuring the thickness as a
234 function of time. After eight days of Ca-carbonate growth, floe thickness was 20 to
235 25 μm , as determined using SEM images of oriented fragments (Fig. 5). In the inset
236 to Fig. 5, a piece of floe collected after four days of growth shown at the same scale
237 has half the thickness of the eight-day growth, suggesting a constant linear growth
238 rate of about 3 $\mu\text{m}/\text{day}$.

239 Sparse florets of hydromagnesite (identified by EDS and morphology) can be
240 found at or partially embedded into the surfaces of calcite rhombs (Suppl. Fig. S5),
241 indicating that hydromagnesite is a trace and late-precipitating phase but can be
242 contemporaneous with calcite growth. Other observed features include co-occurring
243 smooth calcite rhomb faces together with rough micro-stepped saddles (Supp. Fig.
244 S6) suggestive of the effects of bacterially exuded bio-polymers (e.g. Lian et al. 2006;
245 Tourney and Ngwenya 2009), associations with apparent bacterial colonies (Supp.
246 Fig. S7) and aragonite needles featuring stacked steps of hexagonal plates (Supp. Fig.
247 S8) that are suggestive of surface nucleation control of growth.

248 From the above observations, we infer the following growth stages for floes
249 forming at the surface of high pH pools:

- 250 1. Nucleation of aragonite crystals, with horizontal sprays of aragonite crystals
251 suspended by surface tension and forming the base for layer formation.

- 252 2. Bundles of aragonite crystals grow parallel to the water surface and downward
253 into the water, forming hemispheres of crystals that merge to form a nearly
254 continuous layer.
- 255 3. After aragonite, blocky rhombohedral calcite crystals form, nestled among
256 aragonite hemispheres. Calcite can be seen overgrowing aragonite needles.
- 257 4. Late, but accompanying calcite growth, precipitation of hydromagnesite,
258 $Mg_5(CO_3)_4(OH_2) \cdot 4H_2O$ (or perhaps a different hydrous Mg-carbonate (Dypingite
259 $Mg_5(CO_3)_4(OH_2) \cdot 5H_2O$)).
- 260 5. Eventually the floe sinks to the bottom of the pool when a mechanical disturbance
261 breaks the surface tension. See the Supplement for a discussion of the limits of
262 surface tension on floe thickness. After sinking to the bottom of the pool, calcite
263 growth can continue, decorating the broken edges of the floe fragments.

264 **4.2 Chemistry of water samples**

265 The concentrations of selected elements in the water samples along with pH are
266 presented in Table 2. The direct samples of springs and of pools have pH in the
267 range of 11.3 to 12, and are characterized by high Ca concentrations (12 to 58 ppm),
268 high K concentrations (0.5 to 7 ppm), and low Mg concentrations (0.07 to 0.35
269 ppm). In contrast, samples of Austin Creek have pH in the range of 7.8 to 9.5 and are
270 characterized by relatively low Ca concentrations (1.2 to 8 ppm), low K (0.06 to 0.7
271 ppm) and high Mg concentrations (41 to 49 ppm). The pool and spring water
272 samples with $pH \geq 11.3$ mostly have very low Mg/Ca molar ratios, less than 0.01,
273 except for two samples of the Wedding Cake pool that have Mg/Ca ratios of 0.34 and
274 4.5. The creek samples have high Mg/Ca ranging from 8.5 to 66, which varies with
275 pH, suggesting mixing between surface water with high Mg/Ca (pH 7-9) with low
276 Mg/Ca spring water (11-12). Mixing models between creek water and spring water
277 fit well the water samples with $pH < 11$ (Fig. 6), indicating that the chemical
278 influence of spring water can be discerned in downstream creek samples.

279 **4.3 Ca isotopic compositions of water samples**

280 The high pH water samples range in $\delta^{44}\text{Ca}$ from 0.02‰ up to 1.23‰. The low
281 end of the range is similar to the $\delta^{44}\text{Ca}$ of upper mantle peridotite (Huang et al.,
282 2010) consistent with the Ca in the springs being derived from the serpentinization
283 of the ultramafic rocks. The sample with the highest Ca concentration (58 ppm,
284 Wedding Cake Seep) also has the lowest $\delta^{44}\text{Ca}$ (0.02 ± 0.06 ‰), while the sample with
285 the lowest Ca concentration (12 ppm, Wedding Cake Pool) has the highest $\delta^{44}\text{Ca}$
286 (1.23 ± 0.06 ‰). This pattern in concentration and $\delta^{44}\text{Ca}$ suggests an effect due to
287 precipitation of Ca-carbonate at the various sampling localities and times. To
288 examine this, the isotopic data for the waters with pH > 11 (F1-F4, F7-F15) are used
289 for Rayleigh distillation calculations, the results of which are shown in Fig. 7A. The
290 slope of the best-fit line to the data ($r^2 = 0.91$, $p < 0.01$) gives a $\Delta^{44}\text{Ca}$ of $-0.76 \pm$
291 0.12 ‰ (95% confid.), indicating that this is the average Ca isotopic fractionation
292 accompanying the removal of Ca^{2+} to Ca-carbonate from the various waters at The
293 Cedars. Below we compare this value to results for $\Delta^{44}\text{Ca}$ derived from direct
294 water/Ca-carbonate differences.

295 **4.4 Calcium isotopic compositions of Ca-carbonate**

296 The Ca isotope compositions of the measured Ca-carbonates fall in a relatively
297 narrow range of $\delta^{44}\text{Ca}$ from -0.77 ‰ to -0.17 ‰ (Table 3), with no correlation with
298 either $\delta^{13}\text{C}$ or $\delta^{18}\text{O}$ (see Supplement Fig. S9). The analyzed Ca-carbonates cover a
299 range of textures and mineralogy. Because of their immediate association with
300 water, the floe samples provide the best opportunities to directly measure
301 fractionation ($\Delta^{44}\text{Ca}$) between Ca-carbonate and dissolved Ca^{2+} arising from
302 crystallization. We analyzed five water-floe pairs (Table 4), three from different
303 pools at the BSC, and one each from the Wedding Cake and from the GPS. The
304 average of all five pairs gives a $\Delta^{44}\text{Ca}$ of -0.75 ± 0.07 ‰ that compares well to the
305 value given above from the Rayleigh distillation calculation (Fig. 7B).

306 4.5 $\delta^{18}\text{O}$ and $\delta^{13}\text{C}$ of Ca-carbonate samples

307 The $\delta^{18}\text{O}$ and $\delta^{13}\text{C}$ data are presented in Table 3 and Tables S1-S3 in the Supplement,
308 and displayed in Fig. 8 along with data for Ca-carbonates from The Cedars analyzed by
309 Meister et al. (2011). The $\delta^{18}\text{O}$ and $\delta^{13}\text{C}$ values of the Ca-carbonates of all textures fall
310 along a roughly 1:1 line, far from the expected composition for Ca carbonate in
311 equilibrium with Cedars water ($\delta^{18}\text{O} \sim -6$ ‰ VPDB). This 1:1 array stretches from
312 highly fractionated, low values of $\delta^{13}\text{C}$ and $\delta^{18}\text{O}$ toward, but not reaching, the
313 composition of atmospheric CO_2 . These characteristics of the $\delta^{18}\text{O}$ and $\delta^{13}\text{C}$ data, which
314 have been observed also in other alkaline springs associated with ultramafic rocks (e.g.
315 Clark et al. 1992, Leleu et al. 2016, Falk et al. 2016) are explored in the modeling
316 described in the discussion below. The Ca-carbonate samples with the lowest $\delta^{18}\text{O}$ and
317 $\delta^{13}\text{C}$ values are floes from BSC. Other floe samples from GPS fall further up the array,
318 while a floe sample from the Wedding Cake pool is near the high end of the array. Ca-
319 carbonate of different occurrences (textures), pool rim material, and snow from pool
320 bottoms, have compositions distributed along the array. The samples from the Wedding
321 Cake (floe and rim materials) are displaced to the left of the main array, while samples of
322 old laminated carbonates (travertine) form a separate parallel array displaced to the right.
323 Samples of snow from a GPS pool (Carb J, Table 2; GPS-1 #1-3, Suppl. Table S1) have
324 the highest $\delta^{18}\text{O}$ of all Ca-carbonate samples.

325 5. Discussion

326 5.1 Floe growth rate

327 The sample of floe material collected after eight days of growth (Fig. 5) had a
328 thickness of ~ 20 μm and provides a constraint on the growth rate of calcium
329 carbonate precipitation represented by floe formation on pool surfaces. The rate of
330 Ca-carbonate growth per square meter is provided by Eq. 1:

$$331 \quad R \text{ (mol/m}^2\text{/s)} = (d \cdot \rho) / (M \cdot t) \quad \text{Eq. 1}$$

332 Where d is the floe thickness (meters), ρ is the floe density (g/m^3) taking into
333 account porosity and the proportions of calcite and aragonite, M is the molecular
334 weight of Ca-carbonate (100.086 g/mole), and t is the time interval of growth

335 (seconds). Given a thickness of $\sim 20 \mu\text{m}$, a growth time of eight days, a porosity of 0
336 to 40% (Fig. 4), and a mineral composition of 80% calcite and 20% aragonite, Eq. 1
337 yields a growth rate range of $4.8 \times 10^{-7} \text{ mol/m}^2/\text{s}$ to $8.0 \times 10^{-7} \text{ mol/m}^2/\text{s}$. From this
338 range in growth rate, an estimate can be made of the aragonite saturation state (Ω)
339 through the equation $R = k(\Omega-1)^n$ where the rate constant k is given for aragonite
340 precipitation by the empirical relation $\ln(k) = 11.54 - 8690/T$ (T = temp. in Kelvin)
341 and the reaction order, n , is 1.7 (Romanek et al. 2011). Applying this equation to the
342 observed growth range above for a temperature of 17.4°C (Morrill et al., 2013)
343 yields a Ω of ~ 9 to 13. This compares well with the Ω estimates made by Morrill et
344 al. (2013) of 13 for BSC (where our growth rate was measured) and 5 for GPS based
345 on measured ion chemistry.

346 The calculated range in growth rate, along with the average apparent $\Delta^{44/40}\text{Ca}$
347 value of $-0.75 \pm 0.07\text{‰}$ derived above is plotted in Fig. 9 for comparison to the
348 experimental data of Tang et al. (2008), to experimental data from Watkins et al.
349 (2017), to data for calcite from natural travertine deposition (Yan et al 2016), and to
350 a theoretical surface reaction kinetic model of DePaolo (2011). The result for The
351 Cedars compares well with the experimental data. The field experiments of Yan et al.
352 (2016) for calcite precipitation on plexiglass slides reached faster growth rates (~ 3
353 to $6 \times 10^{-6} \text{ cm}^2/\text{s}$) in the case of their canal site and yielded a $\Delta^{44/40}\text{Ca}$, again
354 consistent the experimental data and model (Fig. 9). However their experiments in
355 pools yielded lower precipitation rates and less negative $\Delta^{44/40}\text{Ca}$ that fall well
356 below the result for The Cedars for a similar growth rate.

357 The inferred growth rate for floe Ca-carbonate has implications for the rate of
358 spring resupply to pools, in particular the main BSC pool. For a Ca concentration of
359 51.7 ppm in the spring water supply of the pool, the growth of each square
360 centimeter of floe to a thickness of $25 \mu\text{m}$ would require between 43 and 53 ml
361 (depending on density/porosity of the floe) of BSC spring water. The pool water
362 beneath floes represented by samples D, E, F and I had a calcium concentration of
363 51.1 ppm that is indistinguishable from the BSC spring sample taken at that time
364 (51.7 ppm). Given the area of the pool (roughly 1.6 m^2), a supply rate of fresh spring

365 water to the pool of ~1 ml/s (or ~85 L/day) would be required in order to maintain
366 both the Ca concentration and Ca isotopic composition. At the Wedding Cake pool,
367 evidently the supply of fresh spring water can be limited relative to Ca-carbonate
368 precipitation, since at times the Ca concentration can be driven down by a factor of
369 ~5 relative to the spring source, and the Ca isotopic composition of the pool can be
370 fractionated (fluid F3 $\delta^{44}\text{Ca} = 1.23\text{‰}$) by Ca-carbonate precipitation.

371 The Ca-carbonate growth rate inferred above is comparable to the expected flux
372 of CO_2 from the atmosphere to the pool water. In a set of BaCO_3 precipitation
373 experiments at $\text{pH} = 10$ using a hydroxide buffer, Usdowski and Hoefs (1986)
374 measured a CO_2 flux of $4.7 \times 10^{-7} \text{ mol/m}^2/\text{s}$, which compared well to their own
375 calculated estimate based on CO_2 diffusivity in water and the $\text{CO}_{2(\text{aq})}$ hydroxylation
376 rate constant. The similarity between this value at $\text{pH} 10$ and our growth rate
377 estimates for samples precipitated at $\text{pH} > 10$ suggests that Ca-carbonate floe
378 precipitation and uptake of atmospheric CO_2 are coupled (see the modeling
379 discussion below).

380 **5.2 Aragonite precipitation**

381 We observed aragonite in all of our samples examined with XRPD or SEM, as did
382 Meister et al. (2011) and O'Neil and Barnes, (1971), including in pool rims, pool
383 snow, pool floes and precipitates from mixed spring/creek waters (Table 1, Fig. 4
384 and 5, Fig. S1-S4). Meister et al. (2011) propose that aragonite at The Cedars is
385 associated with high Mg/Ca molar ratios of the water resulting from mixing of high
386 Mg/Ca ratio creek water with the low Mg/Ca spring water leading to a high enough
387 Mg/Ca ratio to inhibit the precipitation of calcite in favor of metastable aragonite.
388 Several direct observations argue against high Mg/Ca as the explanation for all
389 occurrences of aragonite at The Cedars. The pools at the BSC produce floes of
390 aragonite/calcite from solutions with very low Mg/Ca ratios (<0.01 , see above and
391 Table 2), with aragonite as the first phase to precipitate followed by calcite (Fig. 4).
392 Likewise, the rims and snow of low Mg/Ca spring pools also contain aragonite. The
393 high pH of spring pools is sensitive to additions of creek water with a pH of 7.8-8.7.
394 Mixing models demonstrate that even with the addition of creek water with Mg/Ca

395 = 21.8, the Mg/Ca of the mixture does not rise above 2 until the pH falls well below
396 11 (Fig. 6). Such pH values are not seen in the Ca-carbonate precipitating spring
397 pools (pH range 11.3-12.0, Table 2). However, there are instances of aragonite
398 occurring at locations where spring water enters the creek directly (e.g. Carb B and
399 Carb C, see Suppl. Figs S2 and S3) where high Mg/Ca may play a role in favoring
400 aragonite over calcite. Such samples, precipitating from clearly mixed spring/creek
401 water (Carbs B and C in Table 3; Carbs S, T, Y and AA in Table S1; Samples labeled
402 “mixed Spr/Cr” in Fig. 7), have C and O isotope compositions distinct from
403 aragonite/calcite samples precipitated from spring water.

404 Alternative chemical variables that potentially can promote aragonite
405 precipitation over calcite from cool springs include high pH and the degree of
406 oversaturation (see review by Jones, 2017). Experiments by Tai and Chen (1998)
407 demonstrate that the favored Ca-carbonate polymorph is a function of solution pH.
408 They found at 24°C that with pH below 10-10.5, vaterite is the favored polymorph to
409 crystallize, while at pH \geq 12-11.8 calcite is dominant, and for pH in the range of 10.5-
410 11.5 aragonite was the dominant polymorph peaking in abundance at pH \sim 11.3.
411 Similar effects of pH on Ca-carbonate polymorphism were found by Matsumoto et al.
412 (2010). The degree of supersaturation has been shown by Kawano et al. (2009) to
413 control polymorphism, with high ($\Omega > 15$ at 20°C) saturation favoring vaterite and at
414 $\Omega < 15$ favoring calcite. However, these experiments were likely conducted at
415 circum-neutral pH (the pH conditions were measured but not given by Kawano et
416 al., 2009) and so may be consistent with the experiments of Tai and Chen (1998) in
417 which at a Ω of ~ 40 and pH < 10 vaterite precipitation was favored. A pH effect on
418 Ca-carbonate polymorphism has also been described for low temperature (0°C)
419 precipitation of Ca-carbonate; ikaite (a hexahydrate of Ca carbonate) results at pH
420 13.4 while at pH 9 vaterite is the sole product, regardless of Ca²⁺/CO₃²⁻ ratio (Hu et
421 al. 2015).

422 From the SEM observations of floes discussed above, the first phase to
423 precipitate is aragonite, followed by calcite. This is consistent with the surface layer
424 of the water having a pH of 11.0-11.5 and a Ω of 9-13 favoring the nucleation of
425 aragonite over calcite. As the layer thickens it encounters a pH > 11.5 and calcite

426 begins to nucleate and grow. In considering the preferred nucleation of aragonite in
427 modern seawater, Sun et al. (2015) conclude based on *ab initio* calculations that
428 aragonite is favored over calcite for Mg/Ca ratios in the solution greater than ~2
429 due to the surface energy effect of Mg incorporation stabilizing aragonite relative to
430 calcite. We speculate that the effect of pH is to change the surface energy of Ca-
431 carbonate nuclei such that the aragonite nucleation rate is maximized at pH 11.0-
432 11.5, whereas calcite nucleation and growth is promoted at higher pH.

433 **5.3 Kinetic modeling of oxygen and carbon isotope fractionation**

434 A significant advance of the past decade has been the development of
435 quantitative models of kinetic isotope effects between precipitating Ca-carbonate
436 crystals and dissolved ions (DePaolo, 2011; Nielsen et al., 2012, 2013; Watkins et al.,
437 2013, 2014, 2017; Devriendt et al., 2017) and between DIC species and water
438 (Devriendt et al., 2017; Chen et al., 2018). Chen et al (2018) developed a model that
439 integrates CO₂ transport, fluid mixing, carbonate system reaction kinetics, and
440 carbonate precipitation, a combination that is necessary to understand alkaline
441 springs like those at The Cedars. This model is informed by extensive experimental
442 and theoretical work on the kinetics and isotope fractionations among DIC species
443 (e.g. Usdowski et al., 1991; Clark et al., 1992; Usdowski and Hoefs, 1993; Zeebe and
444 Wolf-Gladrow, 2001; Beck et al., 2005; Kim et al., 2006; Zeebe, 2014; Sade and
445 Halevy, 2017) and carbonate minerals (Romanek et al., 1992; Kim et al., 2007;
446 Wolthers et al., 2012; Watkins et al., 2013, 2014). In this section, we present a model
447 adapted from that of Chen et al. (2018), and use it to evaluate the observed C and O
448 isotopic variations, while also using the constraints we have on carbonate growth
449 rates and Ca isotopic compositions.

454 HCO_3^- with subsequent rapid and near-
455 quantitative conversion to CO_3^{2-} . The precipitation of Ca carbonate to build the floes

456 consumes much of the DIC coming from the atmosphere. The isotopic composition
457 of the DIC (essentially all in the form of CO_3^{2-}) is set by hydroxylation of the
458 incoming atmospheric CO_2 to extremely low $\delta^{13}\text{C}$ and $\delta^{18}\text{O}$ values, and remains at
459 such values unless shifted by the addition of DIC from spring water or creek water.

460 As the floe thickens, it eventually detaches and sinks, carrying with it some of the
461 low $\delta^{13}\text{C}$ and $\delta^{18}\text{O}$ surface water into the deeper pool. Hence, the deeper pool water
462 from which the “snow” and rim carbonates precipitate obtains some of its DIC from
463 the boundary layer near the surface either by diffusion or by the fluid boundary
464 layer physically detaching, sinking, and mixing with the deep water. Isotopic
465 equilibration of the detached layer is hindered by the high pH of the pool water, so
466 the kinetic signature of the surface processes can be preserved for a long period of
467 time—days to tens of days at pH = 11.5 (Usdowski et al., 1991).

468 This conceptual framework is used to construct a two-stage model for what is
469 happening at The Cedars (Fig. 11). The first stage, hereafter referred to as the thin-
470 film model, focuses on the diffusional boundary layer ($\sim 100\ \mu\text{m}$) at the pool-
471 atmosphere interface. We solve a system of reaction-diffusion equations to compute
472 the concentrations and isotopic compositions of DIC species throughout the one-
473 dimensional model domain. The results place constraints on the hydroxylation
474 kinetic fractionation factors (note that $\text{KFF} = (\alpha - 1) \cdot 1000$), which are used for
475 defining the isotopic composition of the equilibrated inorganic carbon ($\text{EIC} = \text{HCO}_3^-$
476 $+ \text{CO}_3^{2-}$; Chen et al., 2018) flux in the second stage. The second stage, hereafter
477 referred to as the box model, describes the isotopic composition of a well-mixed
478 reservoir as a function of the following fluxes with distinct isotopic compositions:
479 (1) an EIC flux from the detached surface layer, (2) a spring replenishment flux, (3) a
480 low-pH (8.7) creek flux, and (4) a CaCO_3 precipitation flux. The box model also
481 includes reactions among DIC species. The results are used to determine the
482 environmental conditions required to produce the full $\delta^{18}\text{O}$ - $\delta^{13}\text{C}$ data array.

483 *5.3.1 Thin-film model*

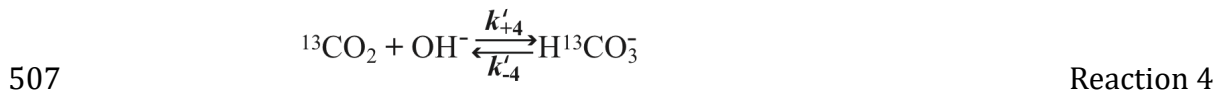
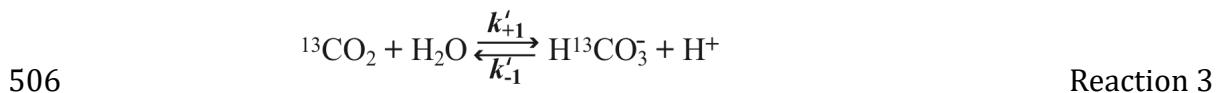
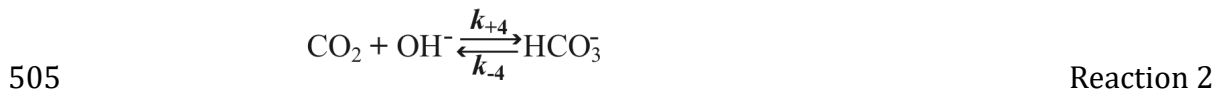
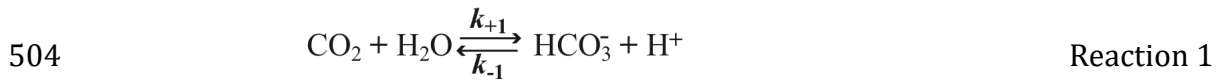
484 For the thin-film model, we start with a pool having a pH of 11.5 and a low DIC
485 concentration of $\sim 0.035\ \text{mM}$, based on the value for a BSC water sample given by

486 Morrill et al. (2013). With these specified pH and DIC values, all other carbonate
 487 parameters are calculated based on expressions given by Zeebe and Wolf-Gladrow
 488 (2001) and p*K* values from Millero et al. (2006). The pool is assumed to be
 489 isotopically equilibrated initially (Table 5) and at saturation with respect to calcite
 490 ($\Omega = 1$), from which we calculate an initial Ca^{2+} concentration of 1.3 mM, in the range
 491 of 0.94 to 1.3 mM reported by Morrill et al. (2013).

492 The rate of CO_2 uptake from the atmosphere is determined by the contrast
 493 between the partial pressure (or fugacity) of the atmospheric CO_2 and the
 494 concentration of $\text{CO}_{2(\text{aq})}$ in the surface water of the pool. The exchange across the
 495 surface between the gas phase CO_2 and the water is assumed to be very fast in
 496 comparison to the diffusive transport of the CO_2 into the pool away from the
 497 surface; i.e., local equilibrium:

$$498 \quad [\text{CO}_2]_{\text{interface}} = K_0 \cdot f_{\text{CO}_2}, \quad \text{Eq. 2}$$

499 where K_0 is Henry's constant (mol/kg-soln/atm) and f_{CO_2} is the fugacity of CO_2
 500 (atm). For a 400 ppm atmosphere, this leads to $[\text{CO}_2]_{\text{eq}} = 1.6 \times 10^{-5}$ moles/kg-soln
 501 which is several orders of magnitude higher than the concentration in the bulk pool.
 502 The incoming CO_2 is converted to HCO_3^- according to the following reactions (cf.
 503 Chen et al. 2018):





512 Rate constants for the ^{18}O substituted species are represented by a for substitution
 513 on H_2O or OH^- , and represented by b for substitution on CO_2 . The factors of $1/3$ and
 514 $2/3$ are necessary for oxygen isotope mass balance. For every mole of $\text{HC}^{18}\text{OO}_2^-$ that
 515 undergoes dehydration, $2/3$ goes to C^{18}OO and $1/3$ goes to H_2^{18}O . Hence, the rate of
 516 change of H_2^{18}O is proportional to $1/3$ of the concentration of $\text{HC}^{18}\text{OO}_2^-$. The same
 517 logic applies to the reverse reaction, and a similar argument can be made for the
 518 (de-)hydroxylation reactions involving $\text{HC}^{18}\text{OO}_2^-$. The ratios of forward to backward
 519 rate constants are equal to the equilibrium constant for each reaction, as given in
 520 Table 6.

521 At high pH (>11), the hydroxylation reactions are much faster than hydration
 522 reactions because OH^- concentration is high. We nevertheless retain the hydration
 523 reactions for completeness. The increase in CO_2 and HCO_3^- at the surface establishes
 524 large concentration gradients that drive diffusion of DIC species downward through
 525 the thin film. At the base of the thin film ($z = -100 \mu\text{m}$), we assume the pool is well-
 526 mixed and able to maintain fixed concentrations of dissolved species. For simplicity
 527 we assume that all dissolved species diffuse at the same rate and that there is no
 528 isotopic fractionation by diffusion (Zeebe, 2011).

529 The combined process of reaction and diffusion is modeled by solving the
 530 following system of partial differential equations:

531
$$\frac{\partial[\text{CO}_2]}{\partial t} = D_{\text{CO}_2} \cdot \frac{\partial^2[\text{CO}_2]}{\partial z^2} + \{-k_{+1}[\text{CO}_2] + k_{-1}[\text{EIC}] \cdot x \cdot [\text{H}^+] - k_{+4}[\text{CO}_2][\text{OH}^-] + k_{-4}[\text{EIC}] \cdot x\} \quad \text{Eq. 3}$$

$$\begin{aligned} \frac{\partial[\text{EIC}]}{\partial t} = & D_{\text{EIC}} \cdot \frac{\partial^2[\text{EIC}]}{\partial z^2} + \{k_{+1}[\text{CO}_2] - k_{-1}[\text{EIC}] \cdot x \cdot [\text{H}^+] \\ & + k_{+4}[\text{CO}_2][\text{OH}^-] - k_{-4}[\text{EIC}] \cdot x\} \end{aligned} \quad \text{Eq. 4}$$

$$\frac{\partial[\text{Ca}^{2+}]}{\partial t} = D_{\text{Ca}} \cdot \frac{\partial^2[\text{Ca}^{2+}]}{\partial z^2} - \text{Sp} \cdot F_{\text{CaCO}_3} \quad \text{Eq. 5}$$

$$\frac{\partial[\text{Alk}]}{\partial t} = D_{\text{Ca}} \cdot \frac{\partial^2[\text{Alk}]}{\partial z^2} - 2 \cdot \text{Sp} \cdot F_{\text{CaCO}_3} \quad \text{Eq. 6}$$

$$\begin{aligned} \frac{\partial[{}^{13}\text{CO}_2]}{\partial t} = & D_{\text{CO}_2} \cdot \frac{\partial^2[{}^{13}\text{CO}_2]}{\partial z^2} + \{-k'_{+1}[{}^{13}\text{CO}_2] + k'_{-1}[{}^{13}\text{EIC}] \cdot {}^{13}x \cdot [\text{H}^+] \\ & - k'_{+4}[{}^{13}\text{CO}_2][\text{OH}^-] + k'_{-4}[{}^{13}\text{EIC}] \cdot {}^{13}x\} \end{aligned} \quad \text{Eq. 7}$$

$$\begin{aligned} \frac{\partial[{}^{13}\text{EIC}]}{\partial t} = & D_{\text{EIC}} \cdot \frac{\partial^2[{}^{13}\text{EIC}]}{\partial z^2} + \{k'_{+1}[{}^{13}\text{CO}_2] - k'_{-1}[{}^{13}\text{EIC}] \cdot {}^{13}x \cdot [\text{H}^+] \\ & + k'_{+4}[{}^{13}\text{CO}_2][\text{OH}^-] - k'_{-4}[{}^{13}\text{EIC}] \cdot {}^{13}x\} + \text{Sp} \cdot F_{\text{CaCO}_3} \cdot \frac{[{}^{13}\text{EIC}]}{[\text{EIC}]} \cdot ({}^{13}\alpha_{\text{CaCO}_3-\text{EIC}}) \end{aligned} \quad \text{Eq. 8}$$

$$\begin{aligned} \frac{\partial[\text{C}^{18}\text{OO}]}{\partial t} = & D_{\text{CO}_2} \cdot \frac{\partial^2[\text{C}^{18}\text{OO}]}{\partial z^2} + \{-b_{+1}[\text{C}^{18}\text{OO}] + \frac{2}{3}b_{-1}[\text{C}^{18}\text{EIC}] \cdot {}^{18}x \cdot [\text{H}^+] \\ & - b_{+4}[\text{C}^{18}\text{OO}][\text{OH}^-] + \frac{2}{3}b_{-4}[\text{C}^{18}\text{EIC}] \cdot {}^{18}x\} \end{aligned} \quad \text{Eq. 9}$$

$$\begin{aligned} \frac{\partial[{}^{18}\text{EIC}]}{\partial t} = & D_{\text{EIC}} \cdot \frac{\partial^2[{}^{18}\text{EIC}]}{\partial z^2} + \{a_{+1}[\text{CO}_2]r_w - \frac{1}{3}a_{-1}[{}^{18}\text{EIC}] \cdot {}^{18}x \cdot [\text{H}^+] \\ & + a_{+4}[\text{CO}_2][{}^{18}\text{OH}^-] - \frac{1}{3}a_{-4}[{}^{18}\text{EIC}] \cdot {}^{18}x \\ & + b_{+1}[\text{C}^{18}\text{OO}] - \frac{2}{3}b_{-1}[{}^{18}\text{EIC}] \cdot {}^{18}x \cdot [\text{H}^+] \\ & + b_{+4}[\text{C}^{18}\text{OO}][\text{OH}^-] - \frac{2}{3}b_{-4}[{}^{18}\text{EIC}] \cdot {}^{18}x\} \\ & + \text{Sp} \cdot F_{\text{CaCO}_3} \cdot \frac{[{}^{18}\text{EIC}]}{[\text{EIC}]} \cdot ({}^{18}\alpha_{\text{CaCO}_3-\text{EIC}}) \end{aligned} \quad \text{Eq. 10}$$

539 where D_i is the diffusivity of species i , χ is the fraction of EIC that is HCO_3^- , F_{CaCO_3} is
540 the growth rate of CaCO_3 (mol/m²/s), Sp is the specific reactive surface area (m²/kg-
541 soln), and r_w is the ¹⁸O/¹⁶O of water. Reaction terms are set apart by braces { }.
542 Following Chen et al. (2018), we write CO_3^{2-} and HCO_3^- together as EIC, assuming

543 instantaneous isotopic equilibration between these two species because they
544 equilibrate on a timescale of 10^{-7} sec (Zeebe and Wolf-Gladrow, 2001). The pH is
545 calculated in the model at each time step from [DIC] and [Alk], assuming
546 instantaneous pH adjustment to these quantities. The time required to establish
547 steady state in the thin film is short, less than 30 seconds, owing to the small length
548 scale of the domain (Supplement Fig. S11).

549 Steady state profiles are displayed in Fig. 12. The only parameter we treat as
550 adjustable is the specific reactive surface area (S_p), which dictates the efficiency of
551 CaCO_3 precipitation. A large S_p implies many crystal nuclei and/or rough crystal
552 surfaces and leads to lower steady state Ω values because a large precipitation flux
553 prevents DIC accumulation (Fig. 12f). In the absence of any constraints on S_p , we
554 report that $S_p \sim 200 \pm 100 \text{ m}^2/\text{kg-soln}$ yields pH, growth rate, and Ω profiles that are
555 most consistent with our estimates based on floe thickness and growth rate
556 calculations (Fig. 12i), but note that a wide range of S_p values (10-1000) can be
557 accommodated by the data.

558 The CO_2 flux from the atmosphere is governed by the concentration gradient of
559 CO_2 , which is very large near the surface since the CO_2 in the water is close to zero
560 (Fig. 12a). The diffusive flux of CO_2 into the deeper pool water is very small because
561 the CO_2 hydroxylates faster than it can diffuse. The increase in DIC and removal of
562 Ca^{2+} to CaCO_3 both lower the pH near the surface (Fig. 12k). Although the pH is
563 lower, the degree of calcite supersaturation is highest near the surface (Fig. 12f)
564 because the increase in DIC more than offsets the DIC speciation effects caused by
565 lower pH.

566 The model accounts for isotopic distillation of reactants as they are converted to
567 products. This is clearly seen in the $\delta^{13}\text{C}$ profile for CO_2 (Fig. 12g) where isotopically
568 light CO_2 has been removed by hydroxylation, leaving behind a residual CO_2 pool
569 with very low concentration that is extremely isotopically heavy. The abrupt return
570 to the initial value at $z = -100$ is a consequence of the fixed concentration boundary
571 condition in the model. Isotopic distillation does not occur for the $\delta^{18}\text{O}$ of CO_2 (Fig.
572 12d) because the KFF is set at 0‰, as discussed further below.

573 5.3.2 CO_2 hydroxylation KFFs

574 The thin-film model is used to inform our estimates of the kinetic fractionation
575 factors (KFFs) related to $\text{CO}_{2(\text{aq})}$ hydroxylation, which represents the instantaneous
576 isotopic fractionation between the reactant $\text{CO}_{2(\text{aq})}$ (for carbon KFF) or ' $\text{CO}_{2(\text{aq})} + \text{OH}^-$ '
577 (for the bulk oxygen KFF) and the product HCO_3^- . To begin, it is important to note
578 that the hydroxylation reaction is essentially unidirectional in the upper 60 μm of
579 the model domain, where the ratio of forward to backward reaction rates is >1000
580 (Fig. 12c). This implies that the full kinetic fractionation is expressed in the EIC prior
581 to it being converted to CaCO_3 . There is, however, an additional kinetic fractionation
582 attending the CaCO_3 precipitation reaction that depends on the degree of
583 supersaturation through an equilibration index E_c (Devriendt et al., 2017). Since the
584 degree of supersaturation is relatively modest for $\text{Sp} > 10 \text{ m}^2/\text{kg}$, the precipitation
585 reaction is bi-directional and the precipitating CaCO_3 is isotopically heavier than
586 CO_3^{2-} . This drives the isotopic composition of EIC to an isotopically lighter
587 composition than that set by the kinetic limit of hydroxylation (Fig. 12e, h, and l),

588 The best-fit hydroxylation KFFs depend on the degree of distillation of EIC as it is
589 converted to CaCO_3 , which in turn depends on Sp (Fig. 12e and 12h). A small Sp
590 leads to a small fraction of the CO_3^{2-} converting to CaCO_3 . In this scenario, the
591 dissolved CO_3^{2-} records the KFF and the CaCO_3 is offset to heavier values (Fig. 12l).
592 By contrast, for $\text{Sp} > 100$, most of the CO_3^{2-} is converted to CaCO_3 and in this
593 scenario, the CaCO_3 records the KFF while the CO_3^{2-} is offset to even lighter values
594 (Fig. 12l). It may be significant that the one measurement of $\delta^{13}\text{C}$ of BSC pool water
595 DIC gives a value of -31.5‰ (VPDB; Morrill et al., 2013), which is about 5‰ lighter
596 than the lightest values recorded by the CaCO_3 and consistent with near complete
597 conversion of CO_3^{2-} to CaCO_3 . This suggests that, instead of the EIC, it is the solid
598 CaCO_3 that records the KFF. If indeed there is a near quantitative transfer of the EIC
599 to CaCO_3 , the carbon and oxygen KFFs estimated from the $\delta^{18}\text{O}$ and $\delta^{13}\text{C}$ of floe
600 samples should be unaffected by their varying proportions of calcite versus
601 aragonite.

602 Using the $\delta^{13}\text{C}$ values of floes at BSC and of local atmospheric CO_2 for the period
603 2013-2018 (NOAA CO_2 station Trinidad Head, USA- White et al. 2015), the carbon
604 KFF related to CO_2 hydroxylation is estimated here to be $-18.1 \pm 0.8\text{‰}$ relative to
605 $\text{CO}_{2(\text{aq})}$. Following the same reasoning as for carbon isotopes, a bulk oxygen KFF is
606 estimated at $-0.4 \pm 1.5\text{‰}$ relative to ' $\text{CO}_{2(\text{aq})} + \text{OH}^-$ '. The oxygen KFF calculated
607 relative to ' $\text{CO}_{2(\text{aq})} + \text{OH}^-$ ' relies on the accuracy of the $\text{OH}^-/\text{H}_2\text{O}$ oxygen EFF. A value of
608 $-21.3 \pm 2.2\text{‰}$ relative to H_2O for the equilibrium isotopic composition of OH^- was
609 used based on quantum-chemical calculations (Zeebe, 2020). Since the isotopic
610 composition of H_2O can be directly measured with high accuracy, and since the OH^-
611 $/\text{H}_2\text{O}$ oxygen EFF is likely to get refined in the future, we also report the KFF relative
612 to the sum of ' $\text{CO}_{2(\text{aq})} + \text{H}_2\text{O}$ ' (KFF* = $-7.1 \pm 0.8\text{‰}$).

613 Kinetic isotope effects of similar magnitude have also been reported for a range
614 of natural and synthetic carbonates formed in high pH solutions with gaseous CO_2 as
615 the main DIC source (Table 7). We reviewed the literature on carbonate minerals
616 precipitated from gaseous CO_2 in high pH solutions to compile a set of carbon and
617 oxygen KFFs within a consistent framework. The revised KFF values listed in Table
618 7 were calculated by taking into consideration the following:

- 619 (i) The temporal and geographical variability in the $\delta^{13}\text{C}$ and $\delta^{18}\text{O}$ of
620 atmospheric CO_2 (Troler et al., 1996; Keeling et al., 2001) for studies
621 where the DIC source was atmospheric CO_2 .
- 622 (ii) $\text{CO}_{2(\text{g})}$ distillation effects were corrected for in (semi-)closed system
623 experiments while an infinite $\text{CO}_{2(\text{g})}$ pool was assumed for fully open
624 experiments.
- 625 (iii) Values for the equilibrium fractionation factors (EFFs) between $\text{CO}_{2(\text{aq})}$
626 and $\text{CO}_{2(\text{g})}$ of -1.1‰ and -0.3‰ were applied for carbon (Vogel et al.,
627 1970) and oxygen (Beck et al., 2005; Barkan and Luz. 2012) isotopes,
628 respectively.

629 For carbon isotopes, laboratory experiments suggest a KFF between -13.7
630 $\pm 0.1\text{‰}$ and $-17.2 \pm 0.6\text{‰}$ (Table 7, Fig. 13a, Craig, 1953; Usdowski and Hoefs, 1986;
631 Clark et al., 1992; Dietzel et al., 2009; Böttcher et al., 2018) while field data suggest a

632 very consistent KFF of between $-16.9 \pm 1.3\text{‰}$ and $-17.2 \pm 0.6\text{‰}$ (Table 7, Fig. 13a;
633 Clark et al., 1992; Mervine et al., 2014; Falk et al., 2016; this study). Some of the
634 disparities could be due to partial re-equilibration (i.e., non-unidirectional
635 hydroxylation reaction), but this is difficult to evaluate. Only three studies suggest a
636 significantly lower carbon KFF than $\sim -17\text{‰}$ (Craig, 1953; open system experiment
637 of Clark et al., 1992; 4°C experiments of Böttcher et al., 2018). Lower apparent KFF
638 may be caused by $\text{CO}_{2(\text{g})}$ - $\text{CO}_{2(\text{aq})}$ disequilibrium when using cold air as a DIC source;
639 Böttcher et al. (2018) conducted their experiments at 4°C while Craig (1953) and
640 Clark et al. (1992) used compressed air (presumably colder than room temperature)
641 in their experiments. Alternatively, the carbon KFF may be negatively correlated
642 with temperature (Fig. 13a, $r^2 = 0.53$, p-value = 0.01), though this hypothesis is not
643 supported by theoretical work (Guo, 2019).

644 For oxygen isotopes, most studies suggest a bulk KFF close to zero or slightly
645 negative expressed relative to the sum of reactants ' $\text{CO}_{2(\text{aq})} + \text{OH}^-$ ' ($-2.8 \pm 1.5\text{‰}$ to
646 $+0.5 \pm 1.1\text{‰}$, Clark et al., 1992; Mervine et al., 2014; Falk et al., 2016; Böttcher et al.,
647 2018; this study). However, the experimental work of Clark et al. (1992) and Dietzel
648 et al. (2009) suggests a negative bulk oxygen KFF of between $-10.0 \pm 0.9\text{‰}$ and -7.9
649 $\pm 0.8\text{‰}$. Although the cause of this discrepancy is unclear, the excellent agreement
650 in the bulk oxygen KFF value among all the field studies and the Böttcher et al.
651 (2018) experimental work at 21°C suggests an oxygen KFF of $-0.2 \pm 0.7\text{‰}$ over the
652 17-28°C temperature range (Fig. 13b). This result is consistent with theoretical
653 calculations for a bulk KFF close to 0‰ (Sade and Halevy, 2017; Guo, 2019).

654 Over the 17-28°C temperature range, the calculated KFF* values average -6.8
655 $\pm 0.8\text{‰}$ when expressed relative to ' $\text{CO}_2 + \text{H}_2\text{O}$ ' (Fig. 13c). The lower KFF* calculated
656 from the experimental result at 5°C (Böttcher et al., 2018) may indicate a positive
657 temperature effect on the KFF of $\sim 0.14\text{‰}/^\circ\text{C}$ but this result will need confirmation
658 with additional data. Such a temperature dependence would be in part caused by
659 the effect of temperature on the $\text{OH}^-/\text{H}_2\text{O}$ oxygen EFF (i.e. $\sim +0.06\text{‰}/^\circ\text{C}$; Zeebe,
660 2020).

661 *5.3.3 Box model for the pools*

662 The thin-film model is useful for quantifying the hydroxylation KFFs and
663 understanding the isotopically light end of the array. To understand the overall
664 trend we consider the different sources of DIC and forms of carbonate precipitating
665 in the pools as a whole. Unlike the thin film at the surface, it takes much longer than
666 30 seconds to establish steady state in the larger volume (10-1000 L) pools. For this
667 part of the system we apply a box model with four fluxes representing the sources
668 and sinks of DIC: (1) an atmospheric flux, (2) a replenishment flux from the spring,
669 (3) a flux from the adjacent low-pH (8.7) creek, and (4) a Ca carbonate precipitation
670 flux. For the atmospheric flux of DIC to the pool (J_{atm}) we use a value of 6×10^{-7}
671 mol/m²/s, based on the steady state EIC gradient in the thin-film model that
672 matches the measured growth rates of the floes. For the replenishment flux (F_{spr}),
673 we use the inferred pool resupply rate of ~ 1 ml/s (see section 5.1). For the CaCO₃
674 precipitation flux, we use the same formulation as in the thin-film model whereby
675 there is a Ω (growth rate) dependence to the isotopic fractionation between CaCO₃
676 and CO₃²⁻ (Devriendt et al. 2017).

677 There are eight differential equations in the box model:

$$678 \quad \frac{\partial [\text{CO}_2]}{\partial t} = \{\text{reaction terms, Eq. 5}\} + \frac{F_{\text{spr}}}{V_{\text{pool}}}([\text{CO}_2]_{\text{spr}} - [\text{CO}_2])$$

$$+ \frac{F_{\text{cr}}}{V_{\text{pool}}}([\text{CO}_2]_{\text{cr}} - [\text{CO}_2]) \quad \text{Eq. 11}$$

$$679 \quad \frac{\partial [\text{EIC}]}{\partial t} = \{\text{reaction terms, Eq. 6}\} + \frac{J_{\text{atm}} \cdot SA_{\text{pool}}}{V_{\text{pool}}}$$

$$+ \frac{F_{\text{spr}}}{V_{\text{pool}}}([\text{EIC}]_{\text{spr}} - [\text{EIC}]) + \frac{F_{\text{cr}}}{V_{\text{pool}}}([\text{EIC}]_{\text{cr}} - [\text{EIC}]) - J_{\text{CaCO}_3} \cdot \text{Sp} \quad \text{Eq. 12}$$

$$682 \quad \frac{\partial [\text{Ca}^{2+}]}{\partial t} = \frac{F_{\text{spr}}}{V_{\text{pool}}}([\text{Ca}^{2+}]_{\text{spr}} - [\text{Ca}^{2+}]) + \frac{F_{\text{cr}}}{V_{\text{pool}}}([\text{Ca}^{2+}]_{\text{cr}} - [\text{Ca}^{2+}]) - J_{\text{CaCO}_3} \cdot \text{Sp} \quad \text{Eq. 13}$$

$$683 \quad \frac{\partial [\text{Alk}]}{\partial t} = \frac{F_{\text{spr}}}{V_{\text{pool}}}([\text{Alk}]_{\text{spr}} - [\text{Alk}]) + \frac{F_{\text{cr}}}{V_{\text{pool}}}([\text{Alk}]_{\text{cr}} - [\text{Alk}]) - 2 \cdot J_{\text{CaCO}_3} \cdot \text{Sp} \quad \text{Eq. 14}$$

685

$$\frac{d[^{13}\text{CO}_2]}{dt} = \{\text{reaction terms, Eq. 9}\} + \frac{F_{\text{spr}}}{V_{\text{pool}}} ({}^{13}R_{\text{CO}_2(\text{spr})} [\text{CO}_2]_{\text{spr}} - [^{13}\text{CO}_2])$$

$$+ \frac{F_{\text{cr}}}{V_{\text{pool}}} ({}^{13}R_{\text{CO}_2(\text{cr})} [\text{CO}_2]_{\text{cr}} - [^{13}\text{CO}_2])$$

$$\frac{d[^{13}\text{EIC}]}{dt} = \{\text{reaction terms, Eq. 10}\} + \frac{J_{\text{atm}} \cdot SA_{\text{pool}}}{V_{\text{pool}}} ({}^{13}R_{\text{EIC}(\text{hydrox})})$$

$$+ \frac{F_{\text{spr}}}{V_{\text{pool}}} ({}^{13}R_{\text{EIC}(\text{spr})} [\text{EIC}]_{\text{spr}} - [^{13}\text{EIC}]) + \frac{F_{\text{cr}}}{V_{\text{pool}}} ({}^{13}R_{\text{EIC}(\text{cr})} [\text{EIC}]_{\text{cr}} - [^{13}\text{EIC}])$$

$$- J_{\text{CaCO}_3} \cdot \text{Sp} \cdot \frac{[^{13}\text{EIC}]}{[\text{EIC}]} \cdot ({}^{13}\alpha_{\text{CaCO}_3\text{-EIC}})$$

$$\frac{d[\text{C}^{18}\text{OO}]}{dt} = \{\text{reaction terms, Eq. 11}\} + \frac{F_{\text{spr}}}{V_{\text{pool}}} ({}^{18}R_{\text{CO}_2(\text{spr})} [\text{CO}_2]_{\text{spr}} - [\text{C}^{18}\text{OO}])$$

$$+ \frac{F_{\text{cr}}}{V_{\text{pool}}} ({}^{18}R_{\text{CO}_2(\text{cr})} [\text{CO}_2]_{\text{cr}} - [\text{C}^{18}\text{OO}])$$

$$\frac{d[^{18}\text{EIC}]}{dt} = \{\text{reaction terms, Eq. 12}\} + \frac{J_{\text{atm}} \cdot SA_{\text{pool}}}{V_{\text{pool}}} ({}^{18}R_{\text{EIC}(\text{hydrox})})$$

$$+ \frac{F_{\text{spr}}}{V_{\text{pool}}} ({}^{18}R_{\text{EIC}(\text{spr})} [\text{EIC}]_{\text{spr}} - [^{18}\text{EIC}]) + \frac{F_{\text{cr}}}{V_{\text{pool}}} ({}^{18}R_{\text{EIC}(\text{cr})} [\text{EIC}]_{\text{cr}} - [^{18}\text{EIC}])$$

$$- J_{\text{CaCO}_3} \cdot \text{Sp} \cdot \frac{[^{18}\text{EIC}]}{[\text{EIC}]} \cdot ({}^{18}\alpha_{\text{CaCO}_3\text{-EIC}})$$

As a reference case, we use $SA_{\text{pool}} = 1 \text{ m}^2$, $\text{Sp} = 0.1 \text{ m}^2/\text{L}$ and $V_{\text{pool}} = 100\text{L}$. This value of Sp is much smaller than the value used in the thin-film model because $V_{\text{pool}} \gg V_{\text{film}}$ and there is a much higher surface area density of CaCO_3 in the thin film than in the bulk pool. The atmospheric DIC flux is $F_{\text{atm}}^* = 6 \times 10^{-7} \text{ mol/s}$, which is much greater than the spring DIC replenishment flux of $F_{\text{spring}}^* = F_{\text{spring}}[\text{DIC}]_{\text{spring}} = 3.5 \times 10^{-8} \text{ mol/s}$, implying that the isotopic results are not sensitive to the $\delta^{13}\text{C}$ of spring water because of its low DIC concentration. The spring flux still plays an important role, however, because it resupplies dissolved Ca^{2+} at a rate of $1.5 \times 10^{-6} \text{ mol/s}$, which is comparable to the DIC flux from the atmosphere.

The results of running the model to steady state for different values of F_{creek}^* at constant F_{atm}^* and F_{spring}^* are displayed in Fig. 14. In each panel there are three

705 curves corresponding to different initial pH values of the pool (Fig. 14a). The change
706 in steady state pH, Ca^{2+} , and [DIC] occurs approximately where F^*_{creek} overtakes
707 F^*_{atm} (Figs. 14a-c). The steady state Ω and surface area normalized growth rate can
708 be tuned by adjusting SA_{pool} , Sp , and V_{pool} (Supplement), but since these parameters
709 have a limited effect on the overall isotopic results, they will not be discussed
710 further.

711 The isotopic results of the box model are displayed in Fig. 15. The light
712 endmember of the array corresponds to low $F^*_{\text{creek}}/F^*_{\text{atm}}$. As the creek DIC flux
713 increases, the pH decreases (shown by red circled numbers for the $\text{pH}_i = 12.0$ case)
714 and the $\delta^{18}\text{O}$ - $\delta^{13}\text{C}$ values move away from the kinetic limit and up the 1:1 line.
715 Importantly, the pH remains above 11 for the entire part of the array below the
716 equilibrium calcite line. The extreme heavy end of the array corresponds to high
717 $F^*_{\text{creek}}/F^*_{\text{atm}}$ and steady state pH values below ~ 11 . A key outcome of mixing of
718 creek DIC to the high pH pool is that the oxygen isotopic composition of HCO_3^- can
719 become isotopically distilled to higher-than-equilibrium values as it is converted to
720 the isotopically lighter CO_3^{2-} . This can account for the cluster of carbonate samples
721 exhibiting higher-than-equilibrium values. The extent of distillation is particularly
722 sensitive to the initial pH, or more generally, the relative alkalinities of the spring
723 versus creek water.

724 In Fig. 15, the CO_2 distillation trajectory illustrates what would occur if all
725 incoming atmospheric CO_2 were to undergo hydroxylation without an opportunity
726 for atmospheric equilibrium exchange. The isotopic data show no evidence to
727 support this, indicating that CO_2 exchanges with, and is replenished by, the
728 atmosphere faster than it is converted to HCO_3^- by hydroxylation. This result
729 supports the local equilibrium assumption in the thin-film model and our treatment
730 in the box model of CO_2 entering the bulk pool as EIC with an isotopic composition
731 reflecting the kinetic limit of CO_2 hydroxylation. The DIC equilibration trajectory
732 shows the isotopic behavior of the EIC as the ratio between HCO_3^- dehydroxylation
733 and CO_2 hydroxylation increases from 0 to 1. The isotopic data show no evidence of
734 partial equilibration, indicating that the HCO_3^- dehydroxylation rate is negligible

735 relative to the CO₂ hydroxylation rate. This is supported by modeling results, which
736 indicate that an unrealistic $V_{\text{pool}}/SA_{\text{pool}} > 1000$ is required in the model framework to
737 yield an appreciable equilibration trajectory (Suppl. Fig. S12).

738 **5.4 Potential paleoenvironmental applications**

739 The samples from old (unknown age) laminated Ca-carbonate from BSC are
740 shifted to the right of the array of modern Ca-carbonates (Fig. 8). A likely
741 explanation is that they formed at a time when atmospheric CO₂ had a heavier, pre-
742 industrial $\delta^{13}\text{C}$ value, as shown schematically in Fig. 8. This feature of the data
743 suggests that the $\delta^{13}\text{C}$ of pre-industrial atmospheric CO₂ may be recoverable from
744 ancient travertine, some of which is as old as 7000 years at The Cedars (¹⁴C ages
745 950-7100 years, Table S4 in the Supplement).

746 The $\delta^{18}\text{O}$ values of old travertines and most modern travertines are close to the
747 end-member $\delta^{18}\text{O}$ value reflecting HCO₃⁻ isotopically equilibrated with creek water
748 (Beck et al., 2005). This suggests surface water DIC is the dominant carbon supply to
749 travertine formation at The Cedars. Hence, old travertines $\delta^{18}\text{O}$ at The Cedars are
750 expected to primarily reflect the oxygen isotope composition of past precipitation
751 and creek water temperature.

752 **5.5 Comparison to Oman carbonates**

753 The $\delta^{13}\text{C}$ - $\delta^{18}\text{O}$ array for the Oman carbonates (Fig. 1) is similar to that for The
754 Cedars. The slopes are indistinguishable but there are two noteworthy differences.
755 First, the lightest $\delta^{18}\text{O}$ value in the Oman array is about 2‰ heavier than at The
756 Cedars despite atmospheric CO₂ having essentially the same isotopic composition in
757 both places. The difference in light isotope limits thus appears to be a consequence
758 of the $\delta^{18}\text{O}$ of H₂O and OH⁻ being about 6‰ higher in Oman, with OH⁻ contributing
759 1/3 of the oxygen to CO₃²⁻ during hydroxylation (Falk et al., 2016). Second, the Oman
760 data is considerably more scattered at the heavy end of the array (Fig. 1). The fact
761 that the data is more tightly clustered at the light end of the array makes sense
762 because the isotopic composition of CO_{2(atm)} does not vary by more than 1-2‰

763 worldwide (Trolrier et al., 1996), and the hydroxylation KFF* only varies by 1.5‰
764 over the 21-32°C range (see section 5.3.2. above). The scatter at the heavy end of the
765 array is most likely due to variable $\delta^{13}\text{C}$ of DIC in alkaline spring waters and other
766 DIC sources over the large area (50 x 200 km) sampled (Falk et al., 2016). By
767 contrast, The Cedars springs lie within a 0.5 km² area where the $\delta^{13}\text{C}$ of DIC is less
768 variable, as evidenced by the tighter clustering of data at the heavy end of the array.

769 **Conclusions**

770 We investigated the textural and isotopic characteristics of carbonates that
771 precipitate from ultrabasic (pH ~ 11-12) spring pools at The Cedars, California. The
772 pools are fed by spring waters that have low [DIC], low Mg/Ca, and relatively high
773 [Ca²⁺] as a consequence of serpentinization and Mg-carbonate precipitation in the
774 subsurface. Once the spring water reaches the surface, CO₂ from the atmosphere
775 enters and a thin film of Ca-carbonate floe crystallizes and is held in place by surface
776 tension. The initial polymorph to crystallize is aragonite, followed by calcite on the
777 underside of the floe as it thickens. The preference of aragonite over calcite in this
778 case is likely controlled by pH not by high Mg/Ca ratio or high supersaturation.

779 Calcium isotopic fractionation between Ca-carbonates and their host solution is
780 sensitive to growth rate. The $\Delta^{44/40}\text{Ca}$ values retrieved from five carbonate-water
781 pairs are indistinguishable, with an average value of $-0.75 \pm 0.07\text{‰}$ ($\pm 95\%$ confid.).
782 The Ca-carbonate growth rates are based on thickness measurements of surface
783 floes of known age and are estimated to be the range of 4.8×10^{-7} mol/m²/sec to
784 8.0×10^{-7} mol/m²/sec. This value is in good agreement with the growth rate
785 dependence of $\Delta^{44/40}\text{Ca}$ determined from laboratory experiments (Tang et al., 2008;
786 Watkins et al., 2017) and modeling (DePaolo, 2011; Nielsen et al., 2012), allowing
787 for differences in temperature and pH.

788 Ca-carbonates display an extreme range (>20‰) in carbon and oxygen isotope
789 compositions. The $\delta^{13}\text{C}$ and $\delta^{18}\text{O}$ values co-vary along a 1:1 line which trends toward
790 the isotopic composition of isotopically equilibrated DIC from surface waters and
791 pointing toward atmospheric CO₂. Most of the samples are lighter in $\delta^{18}\text{O}$, some by
792 as much as 15‰, than the expected equilibrium value at 17.4°C. The extreme light

794 HCO_3^- . The HCO_3^- rapidly deprotonates and is nearly
795 quantitatively converted to CO_3^{2-} ions, which then reacts with Ca^{2+} to precipitate
796 CaCO_3 . We estimate the hydroxylation KFF's to be about -17‰ relative to $\text{CO}_{2(\text{aq})}$ for
797 carbon ($\delta^{13}\text{C}$) and -7‰ relative to ' $\text{CO}_{2(\text{aq})} + \text{H}_2\text{O}$ ' for oxygen ($\delta^{18}\text{O}$). These compare
798 favorably to other estimates based on analysis of natural samples, but discrepancies
799 remain between field and laboratory studies.

800 We adapted the kinetic isotopic fractionation model from Chen et al. (2018) to
801 further investigate mechanisms of Ca-carbonate precipitation and kinetic isotope
802 fractionation. The DIC in solution evolves chemically and isotopically according to
803 the reaction rate equations in the DIC-water- CaCO_3 system. Using known (or
804 reasonably well constrained) isotope-specific reaction rate constants, along with
805 values for the fluxes that are constrained from the literature and our own
806 measurements, the model reproduces the 1:1 co-variation if (1) the residence time
807 of DIC in solution is much shorter than the equilibration time; (2) CO_2 exchange with
808 the atmosphere is efficient so that the incoming CO_2 does not become isotopically
809 distilled when being converted to HCO_3^- ; and (3) the isotopic composition of the
810 isotopically equilibrated spring and creek waters also lies near the 1:1 line defined
811 by the composition of atmospheric CO_2 and the isotopically lightest data points. The
812 model can also match the observation that some of the carbonates are isotopically
813 heavier than the equilibrium value, owing to isotopic distillation of HCO_3^- from creek
814 water as it is nearly quantitatively converted to CO_3^{2-} during mixing with pool water.

815 **Acknowledgements**

816 We are grateful to Roger Raiche for access and transport to The Cedars and for
817 guiding us to the various fascinating spring features at The Cedars. We thank Shaun
818 T. Brown for his occasional assistance in the field, and for his advice on Ca isotopic
819 measurement. We gratefully thank Peter Kelemen (Columbia Univ.) for providing
820 the ¹⁴C ages of travertine samples reported in the Supplement. This research was
821 supported by the US Department of Energy, Office of Science, Office of Basic Energy
822 Sciences under Award No. DE-AC02-05CH11231 to Lawrence Berkeley National
823 Laboratory.

824 **References**

- 825 Adkins J. F., Boyle E. A., Curry W. B. and Lutringer A. (2003) Stable isotopes in deep-
826 sea corals and a new mechanism for “vital effects”. *Geochim. Cosmochim. Acta* **67**,
827 1129–1143.
- 828 Barkan, E. and Luz, B. (2012), High-precision measurements of ¹⁷O/¹⁶O and ¹⁸O/¹⁶O
829 ratios in CO₂. *Rapid Commun. Mass Spectrom.* **26**, 2733-2738. doi:10.1002/rcm.6400
- 830 Barnes, I., LaMarche V. C. and Himmelberg G. (1967) Geochemical evidence of
831 present-day serpentinization. *Science* **156**, 830-832.
- 832 Barnes, I. and O’Neil, J. (1969) The Relationship between Fluids in Some Fresh
833 Alpine-Type Ultramafics and Possible Modern Serpentinization, Western United
834 States. *Geol. Soc. of Amer. Bull.* **80**, 1947-1960.
- 835 Barnes, I., O’Neil, J. and Trescases, J. J. (1978) Present day serpentinization in New-
836 Caledonia, Oman and Yugoslavia. *Geochim. Cosmochim. Acta* **42**, 144-145.
- 837 Beck, W. C., Grossman, E. L. and Morse, J. W. (2005) Experimental studies of oxygen
838 isotope fractionation in the carbonic acid system at 15°, 25°, and 40°C. *Geochim.*
839 *Cosmochim. Acta* **69**, 3493-3503.
- 840 Blake, M. C., Jr., Graymer, R. W. and Stamski, R. E. (2002) Geologic map and map
841 database of western Sonoma, northernmost Marin, and southernmost Mendocino
842 Counties, California: U.S. Geological Survey Miscellaneous Field Studies Map MF-
843 2402, version 1.0, scale 1:62,500.
- 844 Blake, M. C., Jr., Bailey, E. H. and Wentworth, C. M. (2012) The Cedars ultramafic
845 mass, Sonoma County, California. U.S. Geological Survey Open-File Report, 2012-
846 1164, 13p.
- 847 Böttcher, M. E., Neubert, N., Escher, P., von Allmen, K., Samankassou, E. and Nägler,
848 T.F. (2018) Multi-isotope (Ba, C, O) partitioning during experimental
849 carbonatization of a hyper-alkaline solution. *Chemie der Erde* **78**, 241-247.
- 850 Bottinga, Y. (1968) Calculation of fractionation factors for carbon and oxygen

851 isotopic exchange in the system calcite-carbon dioxide-water. *J. Phys. Chem.* **72**, 800-
852 808.

853 Chen, S., Gagnon, A. C. and Adkins, J. F. (2018) Carbonic anhydrase, coral calcification
854 and a new model of stable isotope vital effects. *Geochim. Cosmochim. Acta* **236**, 179-
855 197.

856 Choi, S. H., Shervais, J. W. and Mukasa, S. B. (2008) Supra-subduction and abyssal
857 mantle peridotites of the Coast Range ophiolite, California. *Contrib. Mineral. Petrol.*
858 **156**, 551-576.

859 Clark, I. D. and Fontes, J.-C. (1990) Palaeoclimatic reconstruction in northern Oman
860 based on carbonates from hyperalkaline groundwaters. *Quat. Res.* **33**, 320-336.

861 Clark I. D. and Lauriol B. (1992) Kinetic enrichment of stable isotopes in cryogenic
862 calcites. *Geochim. Cosmochim. Acta* **102**, 217-228.

863 Clark, I. D., Fontes, J.-C., Fritz, P. (1992) Stable isotope disequilibria in travertine
864 from high pH waters: Laboratory investigations and field observations from Oman.
865 *Contrib. Mineral. Petrol.* **56**, 2041-2050.

866 Coleman, R. G. (2000) Prospecting for ophiolites along the California continental
867 margin. In *Ophiolites and Oceanic Crust: New Insights from Field Studies and the*
868 *Ocean Drilling Program*. Dilek, Y. M., Moores, E. M., Elthon, D. and Nicolas, A., eds.
869 Geological Society of American Special Paper 349, p.351-364.

870 Coplen, T. B. (2007) Calibration of the calcite-water oxygen-isotope
871 geothermometer at Devils Hole, Nevada, a natural laboratory. *Geochim. Cosmochim.*
872 *Acta* **71**, 3948-3957.

873 Craig, H., 1953. The geochemistry of the stable carbon isotopes. *Geochim.*
874 *Cosmochim. Acta* **3**, 53-92.

875 Daëron, M.; Guo, W.; Eiler, J.; Genty, D.; Blamart, D.; Boch, R.; Drysdale, R.; Maire, R.;
876 Wainer, K. and Zanchetta, G. (2011) (CO)-C-13-O-18 clumping in speleothems:
877 Observations from natural caves and precipitation experiments. *Geochim.*
878 *Cosmochim. Acta* **75**, 3303-3317.

879 Daëron, M.; Drysdale, R. N.; Peral, M.; Huyghe, D.; Blamart, D.; Coplen, T. B.; Lartaud,
880 F. and Zanchetta, G. (2019) Most Earth-surface calcites precipitate out of isotopic
881 equilibrium. *Nature Comm.* **10**, article 429 doi:10.1038/s41467-019-08336-5

882 DePaolo, D. J. (2011) Surface kinetic model for isotopic and trace element
883 fractionation during precipitation of calcite from aqueous solutions. *Geochim.*
884 *Cosmochim. Acta* **75**, 1039-1056.

885 Devriendt, L. S., Watkins, J. M. and McGregor, H. V. (2017) Oxygen isotope
886 fractionation in the CaCO₃-DIC-H₂O system. *Geochim. Cosmochim. Acta* **214**, 115-
887 142.

888 Dietzel M., Tang J., Leis A. and Köhler S. J. (2009) Oxygen isotopic fractionation
889 during inorganic calcite precipitation – effects of temperature, precipitation rate and
890 pH. *Chem. Geol.* **268**, 107-115.

891 DOE (1994) Handbook of methods for the analysis of the various parameters of the
892 carbon dioxide system in seawater; version 2. ORNL/CDIAC.

893 Falk, E. S., Guo, W., Paukert, A. N., Matter, J. M., Mervine E. M. and Kelemen, P. B.
894 (2016) Controls on the stable isotope compositions of travertine from hyperalkaline
895 springs in Oman: Insights from clumped isotope measurements. *Geochim.
896 Cosmochim. Acta* **192**, 1-28.

897 Guo, W. (2019) Kinetic clumped isotope fractionation in the DIC-H₂O-CO₂ system:
898 patterns, controls and implication. *Geochim. Cosmochim. Acta* **268**, 230-257.

899 Harms, P.A. (2015) Distribution of Tritium in Precipitation and Surface Water in
900 California. MS Thesis, Calif. State Univ. East Bay

901 Hermoso, M.; Horner, T. J.; Minoletti, F. and Rickaby, R. E. M. (2014) Constraints on
902 the vital effect in coccolithophore and dinoflagellate calcite by oxygen isotopic
903 modification of seawater. *Geochim. Cosmochim. Acta* **141**, 612-627

904 Hu, Y.-B., Wolthers, M., Wolf-Gladrow, D. A. and Nehrke, G. (2015) Effect of pH and
905 phosphate on calcium carbonate polymorphs precipitated at near-freezing
906 temperature. *Crystl. Grwth. Design* **15**, 1596-1601.

907 Huang, S., Farkas, J. and Jacobsen, S. B. (2010) Calcium isotopic fractionation
908 between clinopyroxene and orthopyroxene from mantle peridotites. *Earth Planet.
909 Sci. Lttrs.* **292**, 337-344.

910 Jones, B. (2017) Review of calcium carbonate polymorph precipitation in spring
911 systems. *Sed. Geol.* **353**, 64-75.

912 Kawano, J., Shimobayashi, N., Miyake, A. and Kitamura, M. (2009) Precipitation
913 diagram of calcium carbonate polymorphs: its construction and significance. *J. Phys.:
914 Condens. Matter* **21**, doi:10.1088/0953-8984/21/42425102

915 Keeling, C. D., Piper, S. C., Bacastow, R. B., Wahlen, M., Whorf, T. P., Heimann, M. and
916 Meijer, H. A. (2001) Exchanges of atmospheric CO₂ and ¹³CO₂ with the terrestrial
917 biosphere and oceans from 1978 to 2000. I. Global aspects, SIO Reference Series, No.
918 01-06, Scripps Institution of Oceanography, San Diego, 88 pages.

919 Kelemen, P.B., Matter, J., Streit, E.E., Rudge, J.F., Curry, W.B. and Blusztajn, J. (2011)
920 Rates and mechanisms of mineral carbonation in peridotite: natural processes and
921 recipes for enhanced, in situ CO₂ capture and storage. *Annual Review of Earth and
922 Planetary Sciences*, **39**, 545-576.

923 Kim S.-T., Hillaire-Marcel C. and Mucci A. (2006) Mechanisms of equilibrium and
924 kinetic oxygen isotope effects in synthetic aragonite at 25 °C. *Geochim. Cosmochim.
925 Acta* **70**, 5790-5801.

926 Kim S.-T., O'Neil J. R., Hillaire-Marcel C. and Mucci A. (2007) Oxygen isotope
927 fractionation between synthetic aragonite and water: influence of temperature and
928 Mg²⁺ concentration. *Geochim. Cosmochim. Acta* **71**, 4704-4715.

929 Kimball, J. B.; Dunbar R. B. and Guilderson, T. P. (2014) Oxygen and carbon isotope
930 fractionation in calcitic deep-sea corals: Implications for paleotemperature
931 reconstructions. *Chem. Geol.* **381**, 223-233.

932 Leleu, T., Chavagnac, V., Delacour, A., Noiriél, C., Ceuleneer, G., Aretz, M.,
933 Rommevaux, C. and Ventalon, S. (2016) Travertine associated with hyperalkaline
934 springs: evaluation as a proxy for paleoenvironmental conditions and sequestration
935 of atmospheric CO₂. *J. Sed. Res.* **86**, 1328-1343.

936 Lian, B., Hu, Q., Chen, J., Ji, J. and Teng, H. H. (2006) Carbonate biomineralization
937 induced by soil bacterium *Bacillus megaterium*. *Geochim. Cosmochim. Acta* **70**, 5522-
938 5535.

939 Matsumoto, M., Fukunaga, T., and Onoe, K. (2010) Polymorph control of calcium
940 carbonate by reactive crystallization using a microbubble technique. *Chem. Eng. Res.*
941 *Design* **88**, 1624-1630.

942 McConnaughey, T. (1989) ¹³C and ¹⁸O isotopic disequilibrium in biological
943 carbonates: I. Patterns. *Geochim. Cosmochim. Acta* **53**, 151-162.

944 Meister, P., Johnson, O., Coresetti, F. and Nealson, K. H. (2011) Magnesium inhibition
945 controls spherical carbonate precipitation in ultrabasic springwater (Cedars,
946 California) and culture experiments. In *Advances in Stromatolite Geobiology*, Lecture
947 Notes in Earth Sciences 131, doi: 10.1007/978-3-642-10415-2_6

948 Mervine, E. M., Humphris, S. E., Sims, K. W., Kelemen, P. B. and Jenkins, W. J. (2014)
949 Carbonation rates of peridotite in the Samail Ophiolite, Sultanate of Oman,
950 constrained through ¹⁴C dating and stable isotopes. *Geochim. Cosmochim. Acta* **126**,
951 371-397.

952 Millero, F. J., Graham, T. B., Huang, F., Bustos-Serrano, H. and Pierrot, D. (2006)
953 Dissociation constants of carbonic acid in seawater as a function of salinity and
954 temperature. *Marine Chemistry*, **100**, 80-94.

955 Mook, W. (1986) ¹³C in atmospheric CO₂. *Netherlands Journal of Sea Research* **20**,
956 211-223.

957 Morrill, P. L., Kuenen, J. G., Johnson, O. J., Suzuki, S., Rietze, A., Sessions, A. L., Fogel, M.
958 L. and Nealson, K. H. (2013) Geochemistry and geobiology of a present-day
959 serpentinization site in California: The Cedars. *Geochim. Cosmochim. Acta* **109**, 222-
960 240.

961 Nielsen, L. C., Druhan, J. L., Yang, W., Brown, S. T. and DePaolo, D. J. (2011). Calcium
962 Isotopes as Tracers of Biogeochemical Processes. In M. Baskaran (Ed.), *Handbook of*
963 *Environmental Isotope Geochemistry* (pp. 105–124). Berlin, Heidelberg: Springer
964 Berlin Heidelberg. http://doi.org/10.1007/978-3-642-10637-8_7

965 Nielsen, L. C., DePaolo, D. J. and De Yoreo, J. J. (2012) Self-consistent ion-by-ion
966 growth model for kinetic isotopic fractionation during calcite precipitation. *Geochim.*
967 *Cosmochim. Acta* **86**, 166-181.

968 Nielsen, L. C., De Yoreo, J. J. and DePaolo, D. J. (2013) General model for calcite
969 growth kinetics in the presence of impurity ions. *Geochim. Cosmochim. Acta* **115**,
970 200-114.

- 971 O'Neil, J. R. and Barnes, I. (1971) C13 and O18 compositions in some fresh-water
 972 carbonates associated with ultramafic rocks and serpentinites: western United
 973 States. *Geochim. Cosmochim. Acta* **35**, 687-697.
- 974 Pinsent, B. R. W., Pearson, L., Roughton, F. J. W. (1956) The kinetics of combination
 975 of carbon dioxide with hydroxide ions. *Trans. Faraday Soc.*, **52(11)**, 1512-1520.
- 976 Romanek, C. S., Grossman, E. L. and Morse, J. W. (1992) Carbon isotopic fractionation
 977 in synthetic aragonite and calcite: effects of temperature and precipitation rate.
 978 *Geochim. Cosmochim. Acta*, **56(1)**, 419-430.
- 979 Romanek, C. S., Morse, J. W. and Grossman, E. L. (2011) Aragonite kinetics in dilute
 980 solutions. *Aquatic Geochemistry* **17**, 339-356.
- 981 Sade, Z. and Halevy, I. (2017) New constraints on kinetic isotope effects during
 982 CO₂(aq) hydration and hydroxylation: Revisiting theoretical and experimental data.
 983 *Geochim. Cosmochim. Acta* **214**, 246-265
- 984 Sade, Z. and Halevy, I. (2018) Corrigendum to "New constraints on kinetic isotope
 985 effects during CO₂(aq) hydration and hydroxylation: Revisiting theoretical and
 986 experimental data" [*Geochim. Cosmochim. Acta* 214 (2017) 246-265]. *Geochim.*
 987 *Cosmochim. Acta*, **225**, 237-240.
- 988 Spero, H. J.; Bijma, J.; Lea, D. W. and Bemis, B. E. (1997) Effect of seawater carbonate
 989 concentration on foraminiferal carbon and oxygen isotopes. *Nature* **390**, 497-500.
- 990 Sun, W., Jayaraman, S., Chen, W., Persson, K. A. and Ceder, G. (2015) Nucleation of
 991 metastable aragonite CaCO₃ in seawater. *Proc.s Natl. Acad. Sci.s* **112**, 3199-3204.
- 992 Suzuki, S., Ishii, S., Wu, A., Cheung, A., Tenney, A., Wanger, G., J Gijs Kuenen, J. G.,
 993 Nealson, K. H. (2013) Microbial diversity in The Cedars, an ultrabasic, ultrareducing,
 994 and low salinity serpentinizing ecosystem. *Proc.s Natl. Acad. Sci.s*, **110(30)**, 15336-
 995 15341.
- 996 Suzuki, S., Ishii, S., Hoshino, T., Rietze, A., Tenney, A., Morrill, P.L., Inagaki, F., Kuenen,
 997 J. G. and Nealson, K. H. (2017) Unusual metabolic diversity of hyperalkaliphilic
 998 microbial communities associated with subterranean serpentinization at The
 999 Cedars. *The ISME Journal* **11**, 2584-2598.
- 1000 Tai, C. Y. and Chen, F. B. (1998) Polymorphism of CaCO₃ precipitated in a constant-
 1001 composition environment. *AIChE Journal* **44**, 1790-1798.
- 1002 Talbot M. R. (1990) A review of the palaeohydrological interpretation of carbon and
 1003 oxygen isotopic ratios in primary lacustrine carbonates. *Chem. Geol.* **80**, 261-279.
- 1004 Tang J., Dietzel M., Böhm F., Kohler S. and Eisenhauer A. (2008) Sr²⁺/Ca²⁺ and
 1005 ⁴⁴Ca/⁴⁰Ca fractionation during inorganic calcite formation: II. Ca isotopes. *Geochim.*
 1006 *Cosmochim. Acta* **72**, 3733-3745.
- 1007 Tourney, J. and Ngwenya, B. T. (2009) Bacterial extracellular polymeric substances
 1008 (EPS) mediate CaCO₃ morphology and polymorphism. *Chem. Geol.* **202**, 138-146.
- 1009 Tremaine, D. M.; Froelich, P. N. and Wang Y. (2011) Speleothem calcite farmed *in*
 1010 *situ*: Modern calibration of δ¹⁸O and δ¹³C paleoclimate proxies in a continuously-
 1011 monitored natural cave system. *Geochim. Cosmochim. Acta* **75**, 4929-4950.

- 1012 Troler, M.; White, J. W. C.; Tans, P. P.; Masarie, K. A. and P. A. Gemery (1996)
1013 Monitoring the isotopic composition of atmospheric CO₂: Measurements from the
1014 NOAA Global Air Sampling Network. *J. Geophys. Res.* **101**, 25,897– 25,916, 1996.
- 1015 Uchikawa, J. and Zeebe, R. E. (2012) The effect of carbonic anhydrase on the kinetics
1016 and equilibrium of the oxygen isotope exchange in the CO₂-H₂O system: Implications
1017 for ¹⁸O vital effects in biogenic carbonates. *Geochim. Cosmochim. Acta* **95**, 15-34.
- 1018 Usdowski, E. and Hoefs, J. (1986) ¹³C/¹²C partitioning and kinetics of CO₂ adsorption
1019 by hydroxide buffer solutions. *Earth Planet. Sci. Ltrrs.* **80**, 130-134.
- 1020 Usdowski E., Michaelis J., Böttcher M. E. and Hoefs J. (1991) Factors for the oxygen
1021 isotope equilibrium fractionation between aqueous and gaseous CO₂, carbonic acid,
1022 bicarbonate, carbonate, and water (19 °C). *Z. Phys. Chem.* **170**, 237–249.
- 1023 Usdowski E. and Hoefs J. (1993) Oxygen isotope exchange between carbonic acid,
1024 bicarbonate, carbonate, and water: A re-examination of the data of McCrea (1950)
1025 and an expression for the overall partitioning of oxygen isotopes between the
1026 carbonate species and water. *Geochim. Cosmochim. Acta* **57**, 3815–3818.
- 1027 Vogel, J., Grootes, P. and Mook, W. (1970) Isotopic fractionation between gaseous
1028 and dissolved carbon dioxide. *Zeitschrift für Physik* **230**, 225-238.
- 1029 Watkins, J. M., Nielsen, L. C., Ryerson, F. J. and DePaolo, D. J. (2013) The influence of
1030 kinetics on the oxygen isotope composition of calcium carbonate. *Earth Planet. Sci.*
1031 *Ltrrs.* **375**, 349-360.
- 1032 Watkins J. M., Hunt J. D., Ryerson F. J. and DePaolo D. J. (2014) The influence of
1033 temperature, pH, and growth rate on the ¹⁸O composition of inorganically
1034 precipitated calcite. *Earth Planet. Sci. Lett.* **404**, 332–343.
- 1035 Watkins, J. M., DePaolo, D. J. and Watson, E. B., 2017. Kinetic fractionation of non-
1036 traditional stable isotopes by diffusion and crystal growth reactions. *Reviews in*
1037 *Mineralogy and Geochemistry*, 82(1), pp.85-125.
- 1038 White, J. W. C., Vaughn, B. H. and Michel S. E. (2015) University of Colorado, Institute
1039 of Arctic and Alpine Research (INSTAAR), Stable Isotopic Composition of
1040 Atmospheric Carbon Dioxide (¹³C and ¹⁸O) from the NOAA ESRL Carbon Cycle
1041 Cooperative Global Air Sampling Network, 1990-2014, Version: 2015-10-26.
- 1042 Wolthers, M., Nehrke, G., Gustafsson, J. P. and Van Cappellen, P. (2012) Calcite
1043 growth kinetics: Modeling the effect of solution stoichiometry. *Geochim.*
1044 *Cosomochim. Acta* **77(15)**, 121-134.
- 1045 Yan, H., Schmitt, A.-D., Liu, Z., Gangloff, S., Sun, H., Chen, J.; and Chabaux, F. (2016)
1046 Calcium isotopic fractionation during travertine deposition under different
1047 hydrodynamic conditions: Examples from Baishuitai (Yunan, SW China). *Chem. Geol.*
1048 **426**, 60-70.
- 1049 Yumol, L. M., Uchikawa, J. and Zeebe, R. E. (2020). Kinetic isotope effects during CO₂
1050 hydration: Experimental results for carbon and oxygen fractionation. *Geochimica et*
1051 *Cosmochimica Acta* **279**, 189-203.

- 1052 Žák, K.; Onac, B. P. and Perşoiu, A., (2008) Cryogenic carbonates in cave
1053 environments: A review. *Quaternary International*, **187(1)**, 84-96.
- 1054 Zeebe, R.E., 2011. On the molecular diffusion coefficients of dissolved CO₂, HCO₃⁻,
1055 and CO₃²⁻ and their dependence on isotopic mass. *Geochimica et Cosmochimica*
1056 *Acta*, 75(9), pp.2483-2498.
- 1057 Zeebe, R. E. (2014) Kinetic fractionation of carbon and oxygen isotopes during
1058 hydration of carbon dioxide. *Geochim. Cosmochim. Acta* **139**, 540-552.
- 1059 Zeebe, R.E., 2020. Oxygen isotope fractionation between water and the aqueous
1060 hydroxide ion. *Geochimica et Cosmochimica Acta* **289**, 182-195.
- 1061 Zeebe, R.E.; Wolf-Gladrow, D.A. (2001) CO₂ in seawater: equilibrium, kinetics,
1062 isotopes. Elsevier Oceanography Series, Vol. 65. Elsevier, Amsterdam. 360p
1063

1064 **Figure Captions**

1065 **Figure 1.** Plot of $\delta^{13}\text{C}$ vs. $\delta^{18}\text{O}$ of carbonates associated with high pH springs in
1066 Oman emanating from ultramafic rocks of the Samail ophiolite. The dashed box
1067 represents the expected range of equilibrium values of $\delta^{13}\text{C}$ and $\delta^{18}\text{O}$ of DIC from
1068 Falk et al. (2016). The data were compiled from Falk et al. (2016), Mervine et al.
1069 (2014), Clark et al. (1992) and Clark and Fontes (1990). The solid grey line
1070 represents a 1 to 1 relationship between $\delta^{13}\text{C}$ and $\delta^{18}\text{O}$.

1071 **Figure 2.** Maps showing the location of The Cedars, the local geology, and sampling
1072 locations (modified after Morrill et al. 2013). Using the nomenclature of Morrill et al.
1073 (2013) BSC=Barnes Spring Complex, GPS=Grotto Pool Springs. The Wedding Cake is
1074 at the NS1 locality above Mineral Falls.

1075 **Figure 3.** Photos of a spring pool adjacent to Austin Creek at the Barnes Spring
1076 Complex (BSC) taken in October, 2018. The left panel shows examples of Ca-
1077 carbonate floe at the pool surface (much floe has been cleared away in sample
1078 collection, giving a view of the pool bottom), Ca-carbonate snow at the bottom of the
1079 pool, the Ca-carbonate rim of the pool where water exits the pool, and old travertine
1080 deposits. The dark outcrops are ultramafic rocks of The Cedars. The right panel
1081 shows a closer view from a different angle of the pool featured in the left panel.

1082 **Figure 4.** SEM images of floe Ca-carbonate from BSC pool surface. **(A)** Image of the
1083 inferred top-side of the floe (Carb D). Texture consists of radiating crystals of
1084 aragonite (identified in XRPD) in a horizontal plane (detail in inset 1), showing in
1085 places a plumose/branching texture (inset 2). Over all the surface of this side is
1086 relatively flat. **(B)** The inferred bottom-side of the floe. To right is an enlargement of
1087 the area in the dashed box in the left panel. Left image show calcite rhombs sitting
1088 on sprays of aragonite crystals. In contrast to the side shown in A, this side is
1089 hummocky and less smooth. In this example, there are open areas between
1090 aragonite sprays representing approximately 10-15% of the area of the floe.
1091 **(C)** SEM image comparing the top and bottom sides of an another example of floe
1092 carbonate (flakes were placed next to each other in opposite orientations) from the
1093 Barnes Complex. In this case the material was collected to preserve the original
1094 orientation of the sample. The top side is relatively smooth showing horizontal
1095 sprays of aragonite crystals, while the bottom side (the side facing down into the
1096 water) shows downward orientated sprays of aragonite crystals with scattered
1097 rhombs of calcite.

1098 **Figure 5.** SEM images showing cross sections of BSC floe material representing
1099 approximately eight days of growth and (inset) four days of growth. The top side is
1100 to the left, and the bottom side (facing down into the pool water) to the right. The 8-
1101 day image indicates a thickness of 20-25 microns, with about half that thickness
1102 after four days growth, suggesting a constant growth rate of ~ 3 microns/day.

1103 **Figure 6.** The pH vs. Mg/Ca molar ratio for samples of Austin Creek, and
1104 creek/spring mixtures. Samples with $\text{pH} \leq 11$ are shown as red circles. Curves
1105 model mixing between BSC Spring water with $\text{pH}=11.8$, and Mg/Ca molar ratio of
1106 0.002 with Austin Ck water taken upstream of the BSC in April at high-flow (upper,

1107 grey curve) and in August near low-flow (lower, black curve). Dashed line for a
1108 Mg/Ca ratio of 2.

1109 **Figure 7. (A)** An ln-ln Rayleigh fractionation model plot for high-pH waters (>11.0)
1110 from The Cedars springs and pools. The value of F (the fraction of Ca remaining) is
1111 based on the water sample with the highest Ca concentration (58 ppm) and lowest
1112 $\delta^{44}\text{Ca}$ (0.02 ± 0.06) from the seep above the Wedding Cake Pool (sample F9). The
1113 slope of the best-fit line gives a fractionation of $-0.76\pm 0.12\text{‰}$ (95% confid.). **(B)**
1114 Summary of the calcium isotope fractionation factors ($\Delta^{44}\text{Ca}$) determined from
1115 carbonate-water pairs (red circles) and the Rayleigh model shown in A for waters
1116 with $\text{pH} \geq 11.0$. Uncertainties shown at $\pm 95\%$ confidence.

1117 **Figure 8.** The carbon and oxygen isotopic compositions of Ca-carbonate samples
1118 from The Cedars. Open circles shows data from Meister et al. 2011. Vertical arrows
1119 along the x-axis show the $\delta^{13}\text{C}$ of total inorganic C (TIC) from pool sample at the BSC,
1120 and TIC for a sample of Austin Creek (Morrill et al. 2013). Shown for reference is the
1121 isotopic composition of atmospheric CO_2 (Pt Arena, CA data from White et al.
1122 (2015)) and an estimate for pre-industrial atmospheric CO_2 . The black line shows
1123 the slope of a 1 to 1 correlation between $\delta^{18}\text{O}$ and $\delta^{13}\text{C}$, and is parallel to the blue
1124 dashed line provided for visual reference.

1125 **Figure 9.** A comparison between field observations at The Cedars to experimental
1126 data at 25°C from Tang et al. (2008) (white circles), experimental data at 25°C and
1127 15°C from Watkins et al. (2017) (red and blue circles respectively), and to data for
1128 field experiments involving Ca-carbonate (calcite only) growth on plexiglass slides
1129 from Yan et al. 2016. The solid blue curve is Model 1 from DePaolo (2011).

1130 **Figure 10.** Conceptual model for the evolution of Ca-carbonate floes at the surface
1131 of high pH waters. Within the water surface layer (not shown to scale) aragonite
1132 nucleation/growth rates are greater than those of calcite, consistent with $\sim\text{pH}=11$
1133 (Tai and Chen 1998). As the aragonite layer thickens down into the water below
1134 with $\text{pH} \geq 11.5$ calcite nucleation/growth rates become greater than aragonite (Tai
1135 and Chen 1998) resulting in overgrowth by calcite rhombs. Through disturbance of
1136 the pool's surface due to wind, falling debris, rain, etc. the surface tension is broken
1137 and the floe sinks to the bottom where continued calcite precipitation can occur.
1138 With the surface cleared, the process of floe formation begins again.

1139 **Figure 11.** Schematic diagram showing how the two stages of the quantitative
1140 model fit together. The thin-film model focuses on processes within the $100\ \mu\text{m}$
1141 diffusional boundary layer at the pool-atmosphere interface and tracks spatial
1142 variations in DIC species' concentrations and isotopic compositions. The box model
1143 focuses on the larger scale of the bulk pools and how the DIC species' concentrations
1144 and isotopic compositions vary as a function of three fluxes: (1) DIC from the thin
1145 film, (2) DIC replenishment from the spring water inflow and outflow, and (3) CaCO_3
1146 precipitation.

1147 **Figure 12.** Results of the thin-film model. Curves represent steady state profiles for
1148 different values of Sp. **(a)-(k)** Dissolved CO_2 is assumed to be in local chemical and
1149 isotopic equilibrium with the atmosphere at $z = 0$. As CO_2 diffuses downward, it

1150 reacts with OH⁻ to form isotopically light EIC, resulting in residual CO₂ that is
1151 isotopically heavy. The increase in DIC near the surface increases the
1152 supersaturation while decreasing the pH. Precipitation of CaCO₃ decreases [Ca²⁺]
1153 and EIC near the surface. **(I)** The light isotope limits of EIC and CaCO₃ are
1154 determined by the KFFs for hydroxylation and the proportion of CO₃²⁻ that gets
1155 converted to CaCO₃. A large Sp implies near complete conversion with concomitant
1156 isotopic distillation of CO₃²⁻ to values lighter than given by the KFF. In this case, the
1157 CaCO₃ records the isotopic composition of hydroxylated HCO₃⁻.

1158 **Figure 13.** Compilation of hydroxylation KFF's. **(A)** The carbon KFF is likely
1159 between -13 and -17‰. **(B)** The oxygen KFF is close to 0, meaning that the isotopic
1160 composition of HCO₃⁻ that forms by hydroxylation is indistinguishable from the
1161 composition of the weighted sum of reactants (CO₂+OH⁻). **(C)** The oxygen KFF* is -
1162 6.8 ±0.8 when expressed relative to 'CO₂+H₂O'.

1163 **Figure 14.** Box model results for pools of high pH water at The Cedars. **(a)-(f)**
1164 Steady state composition of the pool as a function of F^{*creek} at fixed F^{*spring} and F^{*atm}.

1165 **Figure 15.** Box model results for pools of high pH water at The Cedars using the
1166 same parameters as in Fig. 14. The carbon and oxygen isotopic composition of
1167 CaCO₃ (red curves) is heavier than the EIC (blue curve) due to partial equilibration
1168 between EIC and CaCO₃. The circles with red numbers represent the pH values along
1169 the pH_{ini} = 12 curve and show that pH remains high along the full array. Higher-
1170 than-equilibrium calcite forms when HCO₃⁻ from the creek gets isotopically distilled
1171 during conversion to CO₃²⁻, which is then inherited by the CaCO₃. The green arrows
1172 show the trajectories of DIC equilibration and CO₂ distillation (all incoming CO₂
1173 converted to HCO₃⁻).
1174

Tables 1-7 are below

Table 1. XRD results for mineral compositions of carbonate samples

Label	Description	Aragonite, %	Calcite, %	Vaterite, %	Hydromagnesite, %	Nitromagnesite, %	Brucite, %	Nesquehonite, %
Carb A	Wedding Cake rim	99.7±0.4	0.27±0.06	n.d.	n.d.	n.d.	n.d.	n.d.
Carb B	New Pool Xtl String	99.7±0.4	0.29±0.05	n.d.	n.d.	n.d.	n.d.	n.d.
Carb H	Floe GPS1	17.8±0.3	82.2±0.5	n.d.	n.d.	n.d.	n.d.	n.d.
Carb I	Floe BSC	21.7±0.6	77.8±0.9	0.5±0.2	n.d.	n.d.	n.d.	n.d.
Carb J	GPS filtered snow (pool 1)	68±0.5	0.14±0.06	n.d.	27.4±0.8	4.5±0.4	n.d.	n.d.
Carb K	GPS filtered snow (pool 2)	25.0±0.2	19.8±0.2	n.d.	49.5±0.5	2.3±0.2	0.5±0.08	3.0±0.1
Carb AA	Mixed spr/ck water at BSC	91.0±0.4	1.30±0.08	n.d.	n.d.	n.d.	7.7±0.4	n.d.
BSC	Floe from pool A, BSC. Powder	91.5±0.2	8.51±0.09	n.d.	n.d.	n.d.	n.d.	n.d.
BSC	Floe from pool A, BSC. Sheet	55.2±0.5	45±3	n.d.	n.d.	n.d.	n.d.	n.d.
PB-C1	Pool B snow, from bottom	86.0±0.8	7.1±0.2	n.d.	n.d.	n.d.	6.8±0.2	n.d.
PB-C2 bulk	Edge pool B, BSC. Whole sample	91.1±0.7	0.53±0.04	n.d.	n.d.	n.d.	8.4±0.6	n.d.
PB-C2 crust	Edge pool B, BSC. Outer surface	46.2±0.2	48.8±0.8	n.d.	n.d.	n.d.	5.0±0.2	n.d.
PE-C2 bulk	Edge pool E, BSC. Whole sample	91.0±0.6	5.9±0.1	n.d.	n.d.	n.d.	3.1±0.09	n.d.
PE-C2 crust	Edge pool E, BSC. Outer surface	77.5±0.4	17.9±0.09	0.6±0.2	n.d.	n.d.	4.1±0.2	n.d.

Table 2. Ca isotopic and chemical compositions of waters from The Cedars.

Label	Location	$\delta^{44}\text{Ca}_{\text{BSE}}, \text{‰}$	$\pm 2\sigma$	Ca, ppm*	K, ppm	Mg, ppm	Na, ppm	Sr, ppb	Mg/Ca molar	pH
F1	GPS pool under floe	0.26	0.16	34.9	6.98	0.07	342	1.41	0.0031	12.0
F2	BC spring	0.18	0.12	51.7	1.22	0.07	49	5.23	0.0020	11.8
F3	Wedding Cake Pool	1.23	0.06	12.2	0.54	34.8	14	0.79	4.53	11.3
F4	BC1 pool under floe	0.16	0.06	51.1	1.36	0.11	50	3.16	0.0033	11.5
F5	Ck inflow to New Pool	0.46	0.12	2.2	0.07	40.8	1.7	1.85	29.9	9.0
F6	New Pool next ppt.s	0.32	0.25	9.5	0.26	31.2	7.0	1.85	5.40	9.9
F7	GPS Upper filtrate	0.83	0.20	17.1	5.88	0.06	306	1.71	0.0057	12.1
F8	GPS spring	0.14	0.07	37.5	6.96	0.07	345	1.60	0.0026	12.1
F9	Wedding Cake seep	0.02	0.06	58.1	0.52	0.35	136	0.97	0.0099	11.4
F10	Pool G	0.50	0.26	39.3	1.27	0.19	57	3.0	0.0081	11.6
F11	Pool C	0.24	0.14	41.8	1.26	0.20	56	3.1	0.0079	11.6
F12	Blue Pool	0.12	0.07	51.0	1.27	0.18	57	3.3	0.0057	11.65
F13	BSC2 10/16	0.16	0.12	54.0	1.26	0.098	56	3.5	0.0030	11.7
F14	Pool E	0.27	0.21	41.7	1.57	0.198	57	3.1	0.0078	11.6
F15	Wedding Cake 9/16	0.14	0.11	47.8	0.76	9.8	20	3.5	0.338	11.3
4/14	Creek above Barnes Cpx			1.2†	0.06	49.0	1.6	1.37	66.0	7.8
8/16	Creek above Barnes Cpx			3.1†	0.10	40.9	4.0	1.83	21.8	8.7
8/13	Creek below Camp			8.0†	0.67	41.1	39	2.17	8.52	9.5

*Ca concentrations by isotope dilution except those marked † that were conducted by Q-ICPMS. Other element concentrations by Q-ICPMS, pH measured in the field.

Table 3. Ca, C, and O isotopic compositions of Ca-carbonates

Label	Description	$\delta^{44}\text{Ca}_{\text{BSE}}$ ‰	$\pm 2\sigma$	$\delta^{13}\text{C}_{\text{VPDB}}$ ‰	$\delta^{18}\text{O}_{\text{VPDB}}$ ‰
Carb A	Wedding Cake rim (4/5/14)	-0.46	0.09	-14.62	-4.24
Carb B	New Pool xtl strings #1 (10/11/14)	-0.17	0.07	-11.78	-3.76
Carb C	New Pool encrustation (10/11/14)	-0.46	0.10	-12.00	-3.65
Carb D	BSC floe, upstream (10/11/14)	-0.77	0.11	-26.48	-19.06
Carb E	BSC floe, middle (10/11/14)	-0.69	0.08	-26.73	-18.32
Carb F	BSC floe, downstream (10/11/14)	-0.52	0.19	-26.66	-18.79
Carb G	New Pool xtl strings #2 (10/11/14)	-0.42	0.11	-12.34	-4.80
Carb H	GPS floe (10/11/14)	-0.38	0.02	-21.39	-13.47
Carb I	BSC large floe sample (10/11/14)	-0.66	0.06	-26.71	-18.71
Carb J	GPS upper filtered carb (10/11/14)	-0.68	0.04	-13.48	-0.36
Carb K	GPS filtered carb (10/11/14)	-0.65	0.07	-13.54	-5.13
Carb L	GPS floe (8/3/13)	-0.41	0.10	-23.04	-14.74
Carb M	Wedding Cake 1cm below rim (10/11/14)	--	--	-14.29	-3.56
Carb N	Wedding Cake 15cm below rim (10/11/14)	--	--	-15.08	-4.58
Carb P	Pool E floe (PE-C1) (10/7/16)	-0.48	0.07	-27.55	-19.58
Carb Q	Wedding Cake Floe (9/2/16)	-0.58	0.11	-17.45	-6.69
Carb R	BSC2 Floe (10/7/16)	-0.52	0.07	-25.50	-18.77

Table 4. Calculated values of Ca isotopic fractionation due to Ca-carbonate precipitation using data from Tables 2 and 3 for floe/water pairs

Observation	$\Delta^{44/40}\text{Ca}$, ‰, $\pm 2s$
Rayleigh model with all high pH waters	-0.76 \pm 0.12
Wedding Cake (CarbQ - F15)	-0.72 \pm 0.16
BSC1 (Ave. of Carbs D,E,F, & I minus F4)	-0.84 \pm 0.11
BSC2 (Carb R-F13)	-0.68 \pm 0.14
BSC Pool E (CarbP-F14)	-0.75 \pm 0.22
GPS1 (CarbL-F1)	-0.67 \pm 0.19
Weighted Average Carb-Water	-0.75 \pm 0.07
Weighted Average all values	-0.75 \pm 0.06

Table 5. Compilation of equilibrium fractionation factors (EFFs; T in Kelvin unless otherwise noted)

Compounds	Equation	α (17.4°C)	Reference
<i>Carbon isotopes</i>			
$\text{CO}_2(\text{g}) - \text{HCO}_3^-$	$-9.483T^{-1} + 1.02389$	0.9913	Mook (1986)
$\text{CO}_2(\text{aq}) - \text{HCO}_3^-$	$-9.866T^{-1} + 1.02412$	0.9902	Mook (1986)
$\text{CO}_3^{2-} - \text{HCO}_3^-$	$-0.867T^{-1} + 1.00252$	0.9995	Mook (1986)
$\text{CO}_2(\text{g}) - \text{Calcite}$	$\exp\left\{\frac{-2.4612 + \frac{7666.3}{T} - \frac{2988000}{T^2}}{1000}\right\}$	0.9886	Bottinga (1968)
<i>Oxygen isotopes</i>			
$\text{CO}_2(\text{aq}) - \text{H}_2\text{O}$	$\exp(2520T^{-2} + 0.01212)$	1.0427	Beck et al. (2005)
$\text{HCO}_3^- - \text{H}_2\text{O}$	$\exp(2590T^{-2} - 0.00189)$	1.0331	Beck et al. (2005)
$\text{CO}_3^{2-} - \text{H}_2\text{O}$	$\exp(2390T^{-2} - 0.00270)$	1.0259	Beck et al. (2005)
$\text{Calcite} - \text{H}_2\text{O}$	$\exp\left(\frac{\frac{17747}{T} - 29.777}{1000}\right)$	1.0318	Coplen (2007), Watkins et al. (2013)
$\text{OH}^- - \text{H}_2\text{O}$	$1/[23.5 - 0.0728(T_c - 25)]$	0.9765	Zeebe (2020)
	or		
$\text{OH}^- - \text{H}_2\text{O}$	$1/[19.1 - 0.0455(T_c - 25)]$	0.9787	Zeebe (2020)

Table 6. Constants and parameters used in the model

Symbol	Meaning	Value	Reference/Note
<i>Part I: Model parameters</i>			
F_{spr}	Spring mass flux	0.001 kg-sol/s	To maintain $[\text{Ca}^{2+}]$, see text
$[\text{DIC}]_{\text{spr}}$	Spring [DIC]	0.035 mM	Morrill et al. (2013)
$[\text{Ca}^{2+}]_{\text{spr}}$	Spring $[\text{Ca}^{2+}]$	1.3 mM	Morrill et al. (2013)
$[\text{Alk}]_{\text{spr}}$	Spring total alkalinity	2.6 mM	Calc. from DIC & pH
$[\text{CO}_2]_{\text{spr}}$	Spring $[\text{CO}_2]_{(\text{aq})}$	1.0×10^{-8} mM	Calc. from DIC & pH
$[\text{EIC}]_{\text{spr}}$	Spring $[\text{HCO}_3^-] + [\text{CO}_3^{2-}]$	0.035 mM	Calc. from DIC & pH
F_{cr}	Creek mass flux	Variable (kg-soln/s)	-
$[\text{DIC}]_{\text{cr}}$	Creek [DIC]	2.9 mM	Morrill et al. (2013)
$[\text{Ca}^{2+}]_{\text{cr}}$	Creek $[\text{Ca}^{2+}]$	0.13 mM	Morrill et al. (2013)
$[\text{Alk}]_{\text{cr}}$	Creek total alkalinity	3.0 mM	Calc. from DIC & pH
$[\text{CO}_2]_{\text{cr}}$	Creek $[\text{CO}_2]_{(\text{aq})}$	0.011 mM	Calc. from DIC & pH
$[\text{EIC}]_{\text{cr}}$	Creek $[\text{HCO}_3^-] + [\text{CO}_3^{2-}]$	2.89 mM	Calc. from DIC & pH
J_{atm}	EIC flux through thin water film	6×10^{-7} moles/m ² /s	Usdowski & Hoefs (1986)
SA_{pool}	Surface area of pool	1 m ²	-
J_{CaCO_3}	Carbonate precipitation rate (moles/m ² /s)	$J_{\text{CaCO}_3} = k_{\text{rate}}(\Omega - 1)^{1.7}$	Romanek et al. (2011)
		$\ln k_{\text{rate}} = 11.54 - (8690/T_K)$	Romanek et al. (2011)
		$\Omega = \frac{[\text{Ca}^{2+}][\text{CO}_3^{2-}]}{K_{\text{SP}}}$	Definition
Sp	Reactive surface area (m ² /kg-soln)	Adjustable parameter	0.01 to 1000
F_{spr}^*	Spring DIC flux (moles/s)	$F_{\text{spr}}^* = F_{\text{spr}} \cdot [\text{DIC}]_{\text{spr}}$	-
F_{cr}^*	Creek DIC flux (moles/s)	$F_{\text{cr}}^* = F_{\text{cr}} \cdot [\text{DIC}]_{\text{cr}}$	-
F_{atm}^*	Atmospheric DIC flux (moles/s)	$F_{\text{atm}}^* = J_{\text{atm}} \cdot SA_{\text{pool}}$	-
$F_{\text{CaCO}_3}^*$	Carbonate DIC flux (moles/s)	$F_{\text{CaCO}_3}^* = J_{\text{CaCO}_3} \cdot Sp$	-
<i>Part II: Reaction rate constants</i>			
χ	Fraction of HCO_3^- in EIC	$\chi = \left(1 + \frac{K_2}{[\text{H}^+]}\right)^{-1}$	K_2 from Millero et al. (2006)
k_{+1}	Rate const. CO_2 hydration (s ⁻¹)	$\log_{10} k_{+1} = 329.85 - 110.54 \log_{10}(T_K) - \frac{17265.4}{T_K}$	Pinsent et al. (1956) Uchikawa and Zeebe (2012)

k_{-1}	Rate const. CO ₂ dehydration (M ⁻¹ s ⁻¹)	$k_{-1}=k_{+1}/K_1$	K_1 from Millero et al. (2006)
k_{+4}	Rate const. CO ₂ hydroxylation (M ⁻¹ s ⁻¹)	$\log_{10} k_{+4} = 13.635 - \frac{2895}{T_K}$	Pinsent et al. (1956) Uchikawa and Zeebe (2012)
k_{-4}	Rate const. CO ₂ dehydroxylation (s ⁻¹)	$k_{-4} = k_{+4} \cdot \left(\frac{K_w}{K_1} \right)$	K_w from DOE (1994)

Table 6 (cont'd). Constants and parameters used in the model

Symbol	Meaning	Value	Reference/Note
<i>Part III: Isotopic parameters</i>			
r_w	$^{18}\text{O}/^{16}\text{O}$ ratio of H_2O	0.00199377	$\delta^{18}\text{O}_{\text{VSMOW}}=-5.7$
r_{CO_2}	$^{18}\text{O}/^{16}\text{O}$ ratio of CO_2	-	Isotope ratio
r_{EIC}	$^{18}\text{O}/^{16}\text{O}$ ratio of EIC	-	Isotope ratio
R_{CO_2}	$[\text{C}^{18}\text{OO}]/[\text{CO}_2]$	$2r_{\text{CO}_2}$	Isotopologue ratio
R_{EIC}	$[\text{EIC}^{18}]/[\text{EIC}^{16}]$	$3r_{\text{EIC}}$	Isotopologue ratio
χ^{13}	Fraction of $\text{H}^{13}\text{CO}_3^-$ in ^{13}EIC	$\chi^{13} = \left(1 + \frac{K_2 \cdot \alpha_{\text{CO}_3^-/\text{HCO}_3^-}}{[\text{H}^+]} \right)^{-1}$	-
χ^{18}	Fraction of $\text{HC}^{18}\text{OO}_2^-$ in ^{18}EIC	$\chi^{18} = \left(1 + \frac{K_2 \cdot \alpha_{\text{CO}_3^-/\text{HCO}_3^-}}{[\text{H}^+]} \right)^{-1}$	-
k'_{+1}	Rate const. for $^{13}\text{CO}_2$ hydration (s^{-1})	$k'_{+1}/k_{+1} = 0.987$	Zeebe & W-G (2001)
k'_{-1}	Rate const. for $^{13}\text{CO}_2$ dehydration ($\text{M}^{-1}\text{s}^{-1}$)	$k'_{+1}/k'_{-1} = K_1 \cdot \alpha_{\text{HCO}_3^-/\text{CO}_2(\text{aq})}$	Equilibrium constraint
k'_{+4}	Rate const. for $^{13}\text{CO}_2$ hydrox. ($\text{M}^{-1}\text{s}^{-1}$)	$k'_{+4}/k_{+4} = 0.9829$	This study
k'_{-4}	Rate const. for $^{13}\text{CO}_2$ dehydrox. (s^{-1})	$k'_{+4}/k'_{-4} = K_1/K_W \cdot \alpha_{\text{HCO}_3^-/\text{CO}_2(\text{aq})}$	Equilibrium constraint
a_{+1}, b_{+1}	Rate const.s for hydration ($\text{M}^{-1}\text{s}^{-1}$)	$a_{+1}/k_{+1} = 1.0000$ $b_{+1}/k_{+1} = 0.9812$	Yumol et al. (2020) [†]
a_{-1}, b_{-1}	Rate const.s for dehydration ($\text{M}^{-1}\text{s}^{-1}$)	$a_{+1}/k_{+1} = K_1 \cdot \alpha_{\text{HCO}_3^-/\text{H}_2\text{O}}$ $b_{+1}/k_{+1} = K_1 \cdot \alpha_{\text{HCO}_3^-/\text{CO}_2}$	Equilibrium constraint Equilibrium constraint
a_{+4}, b_{+4}	Rate const.s for hydrox. ($\text{M}^{-1}\text{s}^{-1}$)	$a_{+4}/k_{+4} = 0.9988$ $b_{+4}/k_{+4} = 1.0000$	This study [‡] This study [‡]
a_{-4}, b_{-4}	Rate const.s for dehydrox. (s^{-1})	$a_{+4}/k_{+4} = \frac{K_1}{K_W} \cdot \frac{\alpha_{\text{HCO}_3^-/\text{H}_2\text{O}}}{\alpha_{\text{OH}^-/\text{H}_2\text{O}}}$ $b_{+4}/k_{+4} = \frac{K_1}{K_W} \cdot \alpha_{\text{HCO}_3^-/\text{CO}_2}$	Equilibrium constraint Equilibrium constraint
$^{13}R_{\text{EIC}(\text{hydrox})}$	Composition of hydroxylated CO_2	18‰ lighter than $\text{CO}_2(\text{atm})$	This study
$^{18}R_{\text{EIC}(\text{hydrox})}$	Composition of hydroxylated CO_2	7.1‰ lighter than 'CO ₂ +OH'	This study

E_c	Calcite- CO_3^{2-} equilibration index	$E_c = \Omega^{-n_2}$, $n_2 = 0.2$	Devriendt et al. (2017)
$^{13}\alpha_{\text{C}/\text{CO}_3^{2-}}$	Growth rate-dependent isotopic fractionation	$\frac{^{13}\alpha_f}{1 + E_c \left(\frac{^{13}\alpha_f}{^{13}\alpha_{\text{eq}}} - 1 \right)}$ where $^{13}\alpha_f = 1.0000$ and $^{13}\alpha_{\text{eq}} = 1.0032$	Devriendt et al. (2017) DePaolo (2011) Watkins and Hunt (2014)
$^{18}\alpha_{\text{C}/\text{CO}_3^{2-}}$	Growth rate-dependent isotopic fractionation	$\frac{^{18}\alpha_f}{1 + E_c \left(\frac{^{18}\alpha_f}{^{18}\alpha_{\text{eq}}} - 1 \right)}$ where $^{18}\alpha_f = 0.9995$ and $^{18}\alpha_{\text{eq}} = 1.0057$	Devriendt et al. (2017) DePaolo (2011)
$^{13}\alpha_{\text{C}/\text{EIC}}$	Growth rate-dependent isotopic fractionation	$^{13}\alpha_{\text{C}/\text{CO}_3^{2-}} \cdot (1 - ^{13}\chi) / (1 - \chi)$	-
$^{18}\alpha_{\text{C}/\text{EIC}}$	Growth rate-dependent isotopic fractionation	$^{18}\alpha_{\text{C}/\text{CO}_3^{2-}} \cdot (1 - ^{18}\chi) / (1 - \chi)$	-

†These values yield a bulk KFF that is consistent with Yumol et al. (2020)

‡These values yield a bulk KFF the is consistent with 'this study' in Table 7.

Table 7. Compilation of CO₂ hydroxylation KFF's

reference	study type	mineral	T (°C)	±	pH	δ ¹³ C (‰ VPDB)				Carbon KFF		δ ¹⁸ O (‰ VSMOW)				Oxygen bulk KFF*					
						CO _{2(g)}	±	mineral	±	vs CO _{2(aq)} ^h	±	H ₂ O	±	CO _{2(g)}	±	mineral	±	vs 'CO _{2(aq)} + OH' ^k	±	vs 'CO _{2(aq)} + H ₂ O' ^k	±
Craig (1953)	Lab.	witherite	20	3	?	-9.1	0.1	-23.1	0.1	-13.7 ⁱ	0.1	-	-	-	-	-	-	-	-	-	-
Usdowski & Hoefs (1986)	Lab.	witherite	18	1	10.0	-7.7 ^a	0.3	-25.7	0.4	-17.0	0.5	-	-	-	-	-	-	-	-	-	-
Clark et al. (1992)	Lab.	witherite	22	2	>11.5	-10.5	0.4	-25.0	1.0	-13.9 ⁱ	1.1	-6.7	0.1	36.6	0.3	6.8	1.0	-8.5	1.4	-15.0	0.2
Clark et al. (1992)	Lab.	witherite	22	2	12.8	-45.2	0.1	-61.3	0.1	-16.2 ⁱ	0.1	-11.9	0.1	11.1	0.1	-11.2	0.1	-7.9	0.8	-14.5	0.1
Dietzel et al. (2009)	Lab.	calcite	5	1	10.5	-	-	-	-	-	-	-9.6	0.1	35.7 ⁱ	0.1	3.4	0.1	-10.0	0.9	-16.8	0.1
Böttcher (2018)	Lab.	witherite	4	1	12.4	-8.6 ^b	0.5	-21.4	0.1	-11.8	0.5	-7.0	0.1	30.9 ^b	1.0	8.3	0.1	-2.8	1.5	-9.8	0.7
Böttcher (2018)	Lab.	witherite	21	1	12.4	-8.6 ^b	0.5	-25.3	0.1	-15.8	0.5	-7.0	0.1	30.9 ^b	1.0	10.0	0.1	-1.5	1.4	-8.1	0.7
Clark et al. (1992)	Field	calcite	28	6	11.5	-7.5	1.1	-24.5 ^c	0.2	-17.0	1.1	-0.5	0.1	31.1 ^b	0.5	14.3 ^c	0.9	0.4	1.4	-6.2	0.4
Clark et al. (1992)	Field	calcite	28	6	11.5	-7.5	1.1	-25.3 ^d	0.7	-16.9	1.3	-0.9	0.1	31.1 ^b	0.5	13.5 ^d	0.1	-0.3	1.0	-6.8	0.4
Mervine et al. (2014)	Field	calcite	28	6	11.0	-8.6 ^b	0.2	-26.5 ^e	0.3	-17.0	0.3	-0.5	1.5	31.1 ^b	0.5	14.4 ^e	0.4	0.5	1.1	-6.0	0.8
Falk et al. (2016)	Field	arag. & calcite	27	5	11.7	-8.6 ^b	0.2	-26.8 ^f	0.6	-17.2	0.6	0.1	1.0	31.1 ^b	0.5	14.0 ^f	0.4	0.0	1.1	-6.6	0.7
this study	Field	arag. & calcite	17	1	11.0	-8.6 ^b	0.4	-26.6 ^g	0.7	-17.1	0.8	-5.7	1.2	30.9 ^b	1.0	11.4 ^g	0.4	-0.4	1.5	-7.1	1.1

*Note: KFFs are expressed as $e = (a-1)1000$

^aKeeling et al. (2001), station La Jolla (CA, USA)

^bNOAA CO₂ global network station closest to study site (incl. 2017 Ochsenkopf, Germany; 2007-2012 Ketura, Israel; 2007-2012 Kaashidhoo, Maldives; 2013-2018 Trinidad Head, USA)

^caverage modern crust 'NJ' samples

^daverage modern crust 'clinic' samples

^eaverage of two lowest 'crust' samples

^faverage of 'WHOI surface film' samples

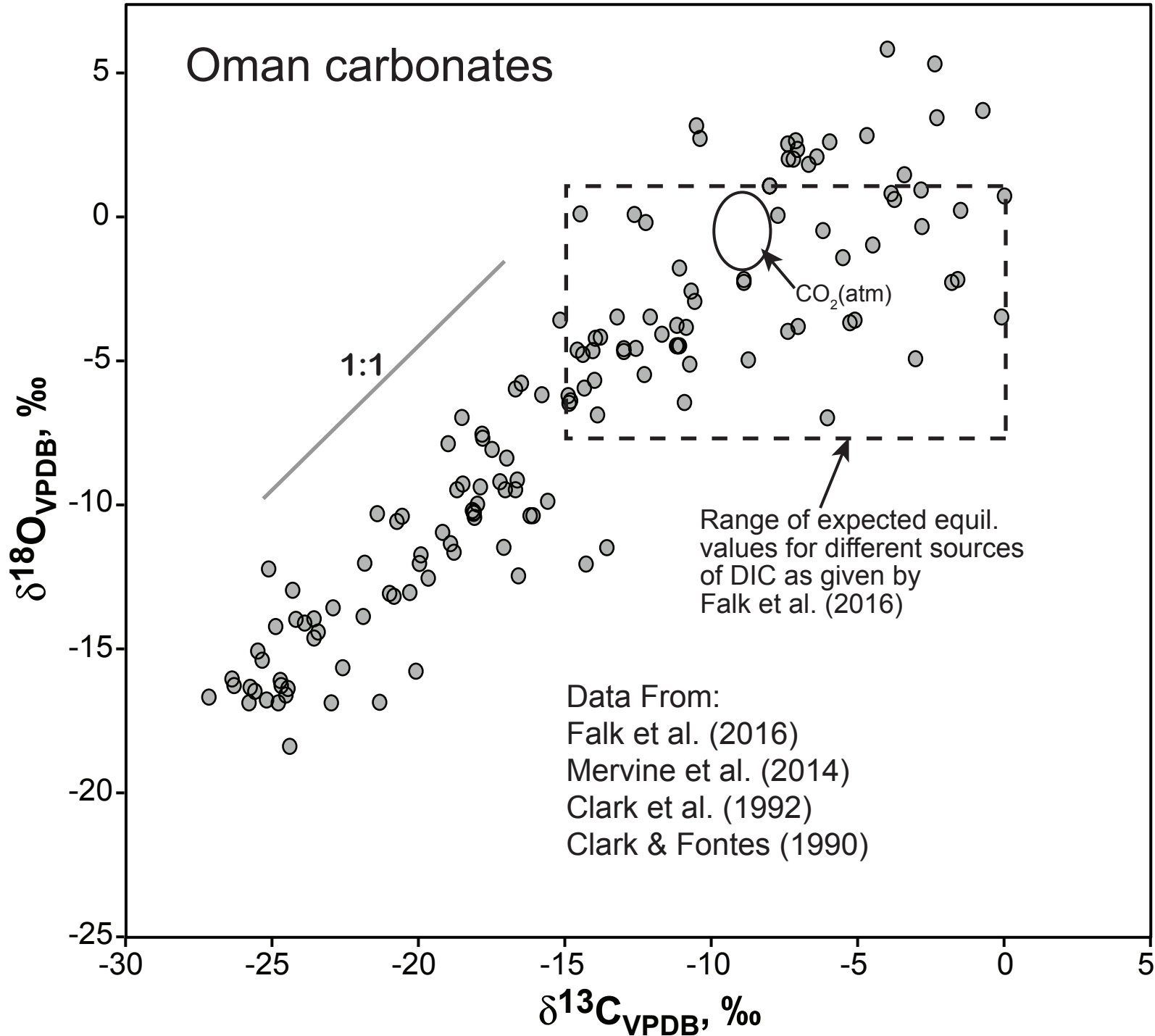
^gaverage 'BSC floes' samples

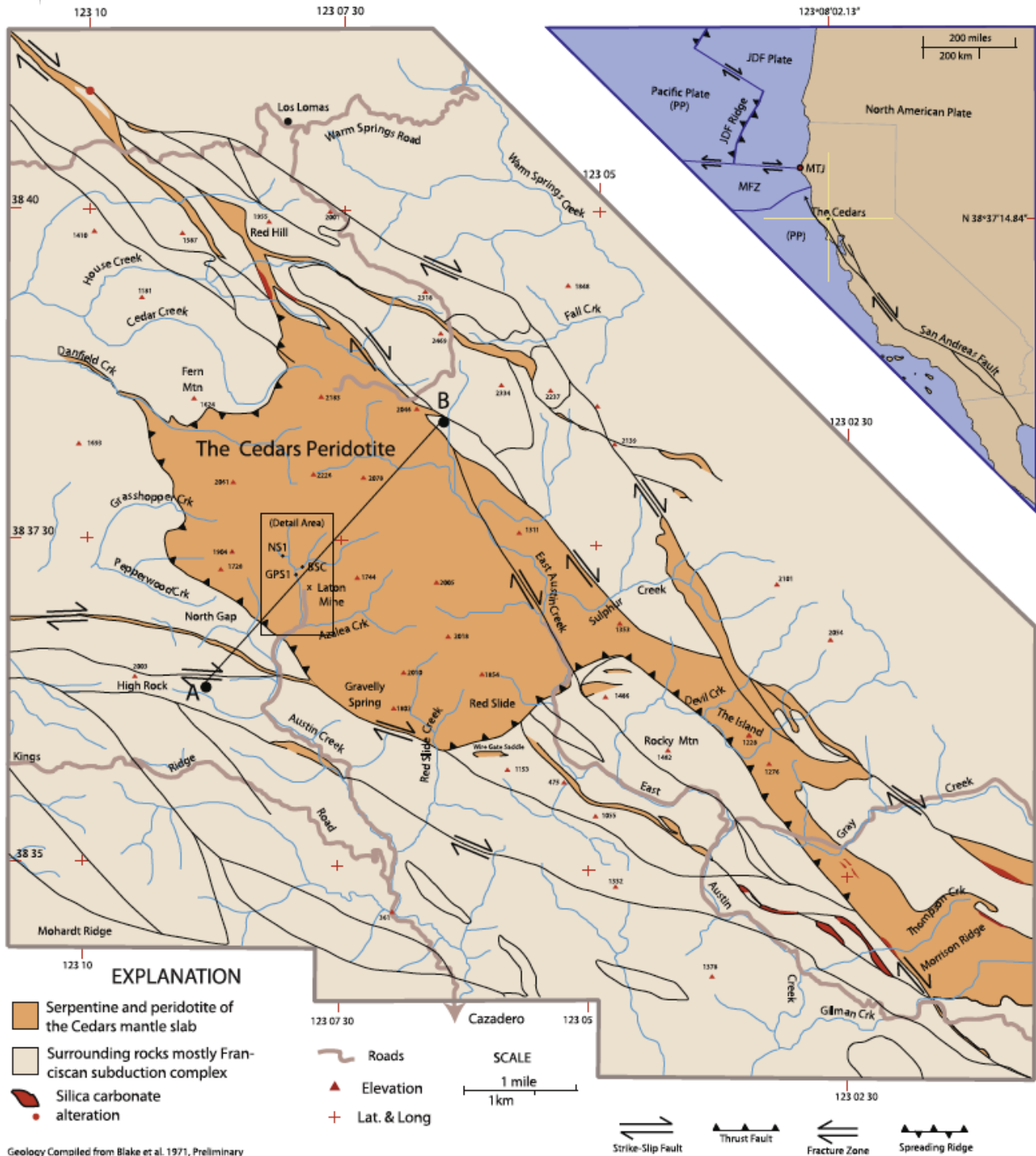
^hCO_{2(aq)}-CO_{2(g)} carbon fractionation of 1.1‰ from Vogel et al. (1970)

ⁱcorrected for distillation effect

^kCO₂-H₂O isotopic equilibrium assumed

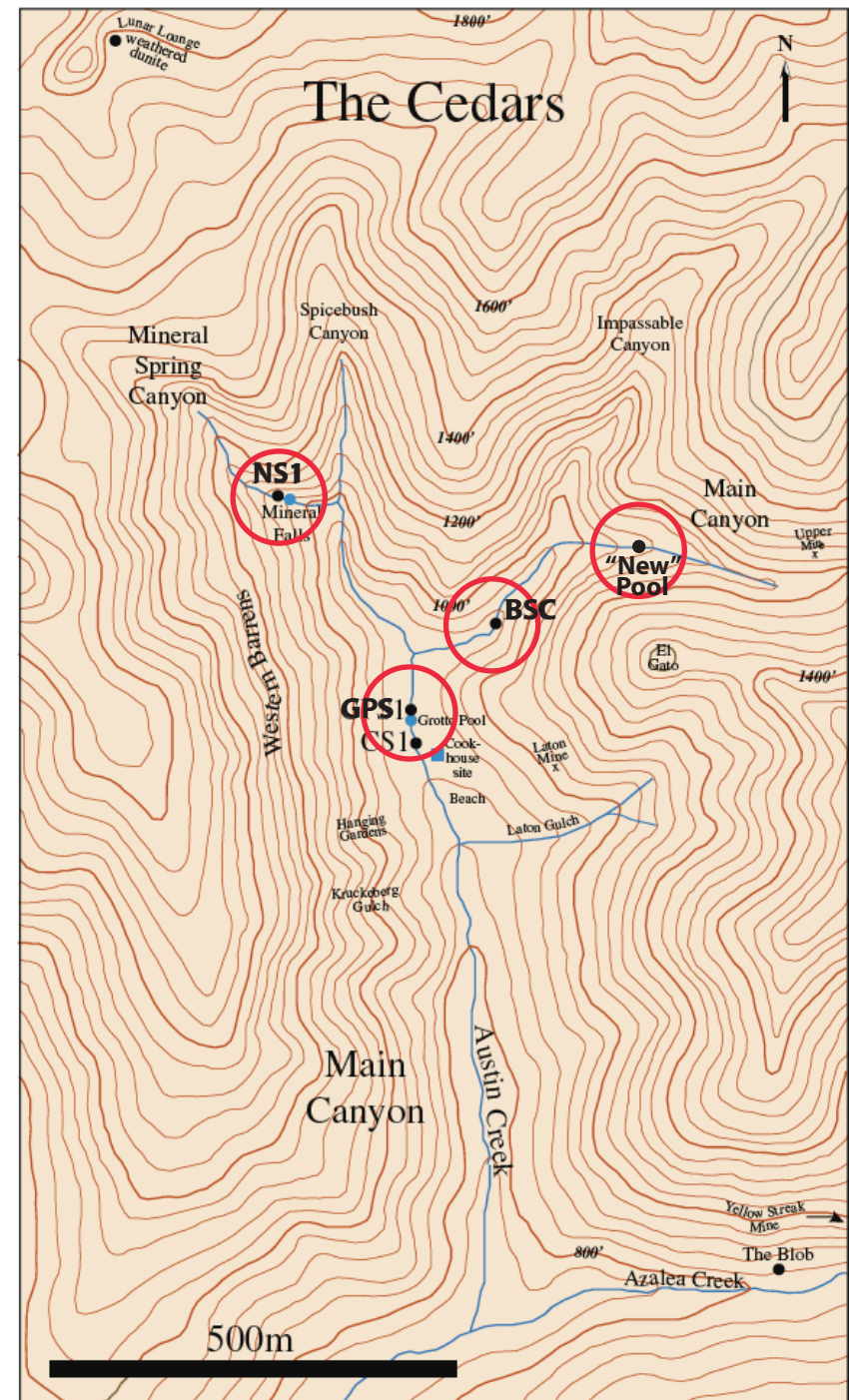
Oman carbonates

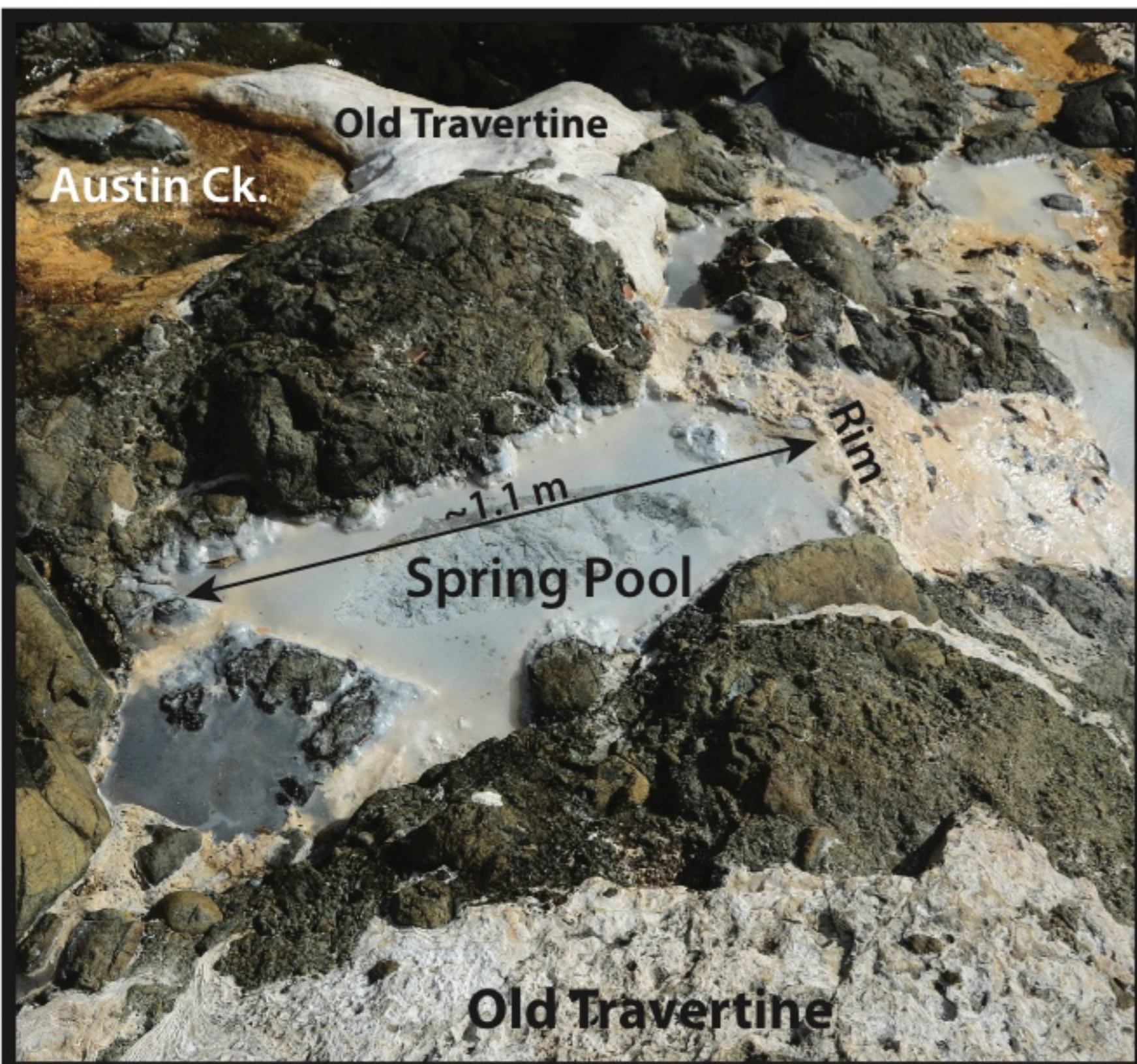


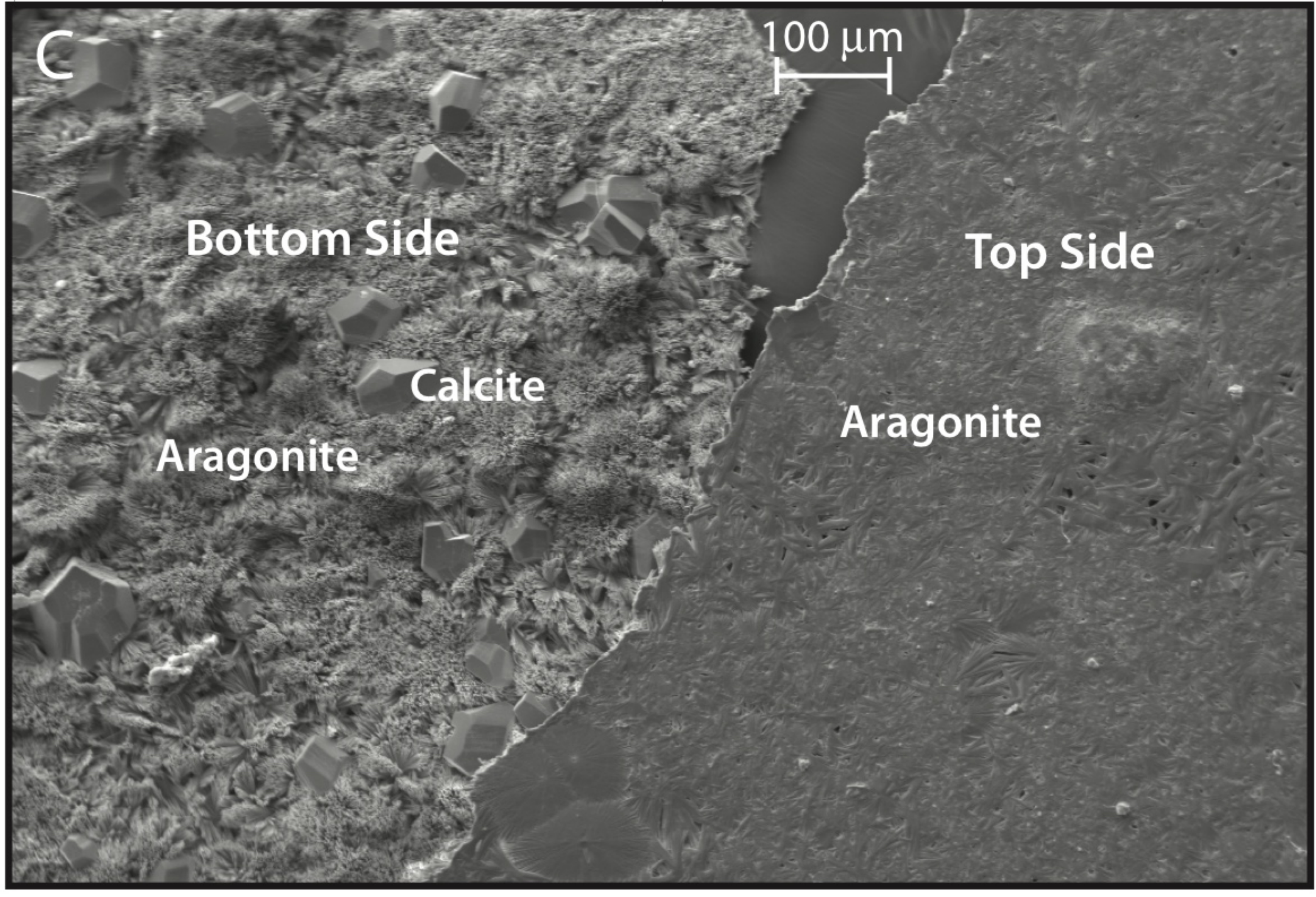
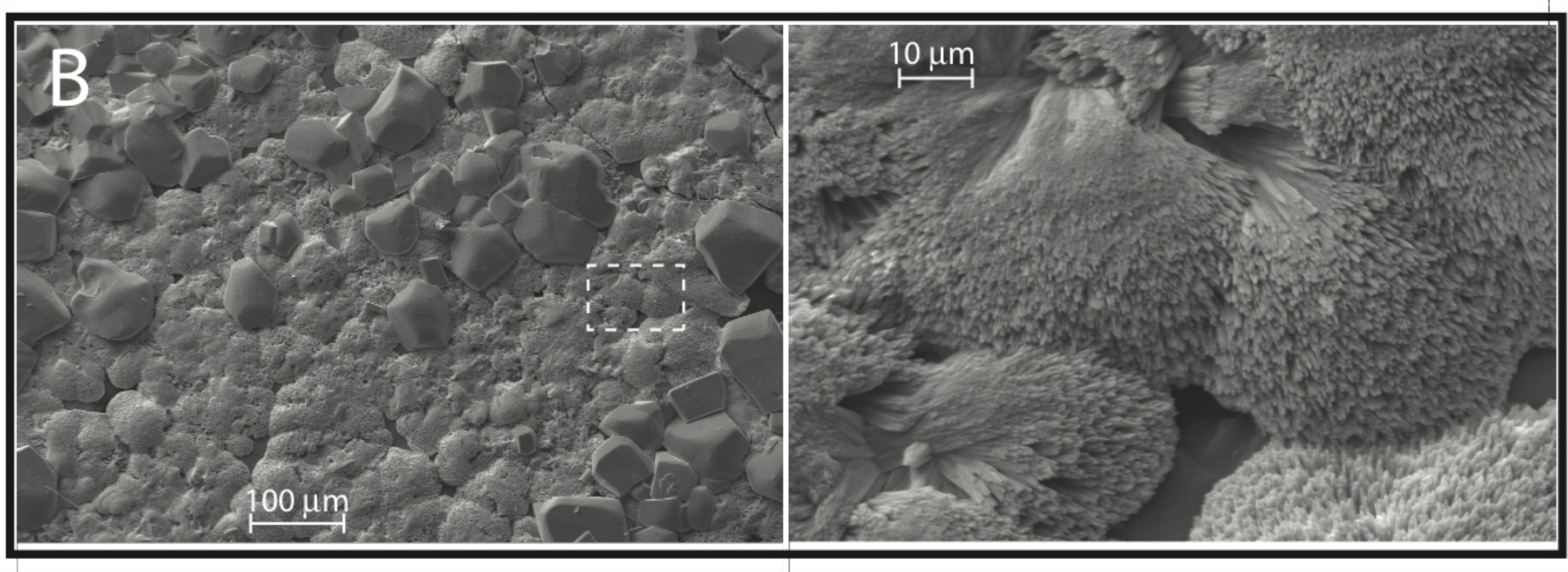
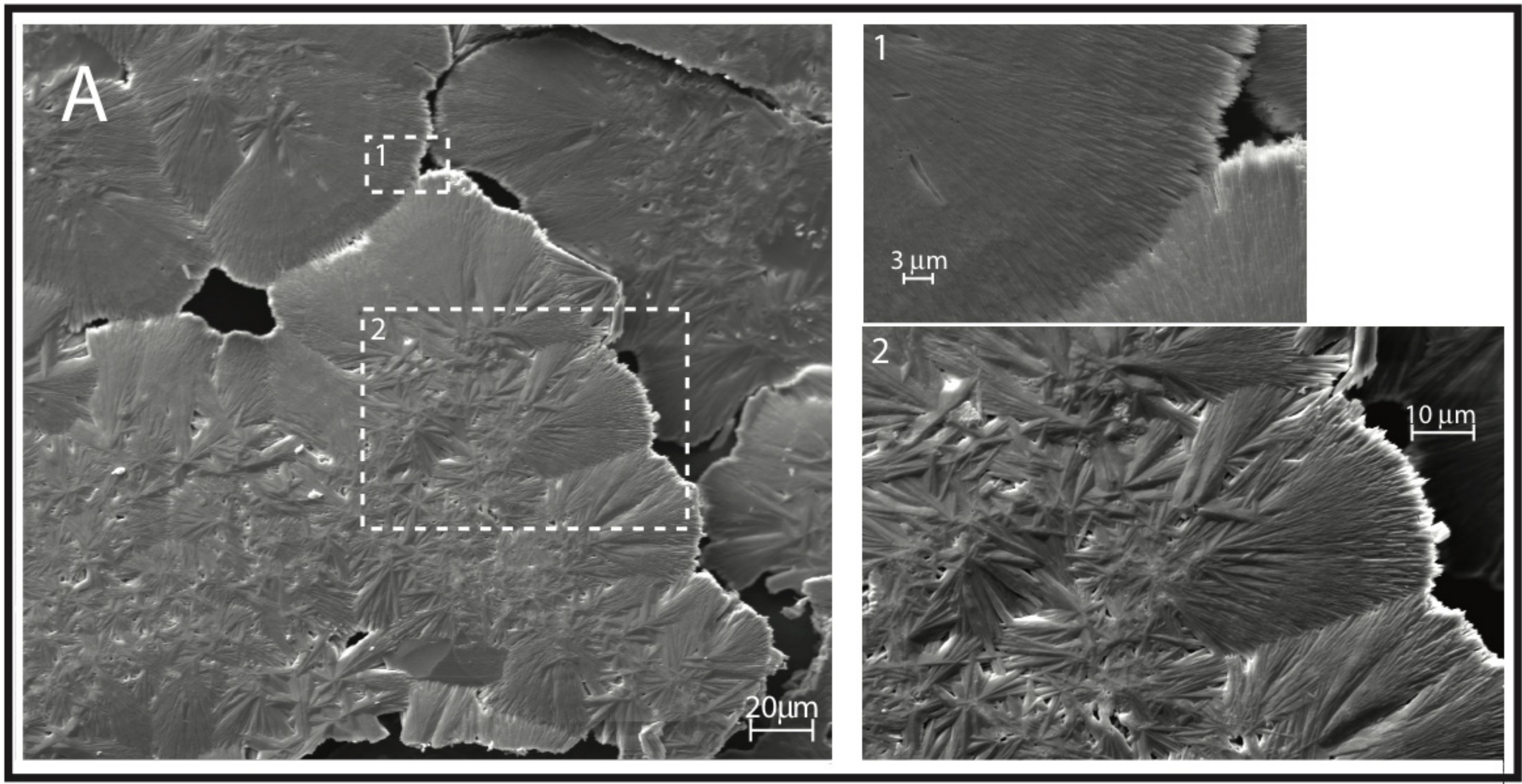


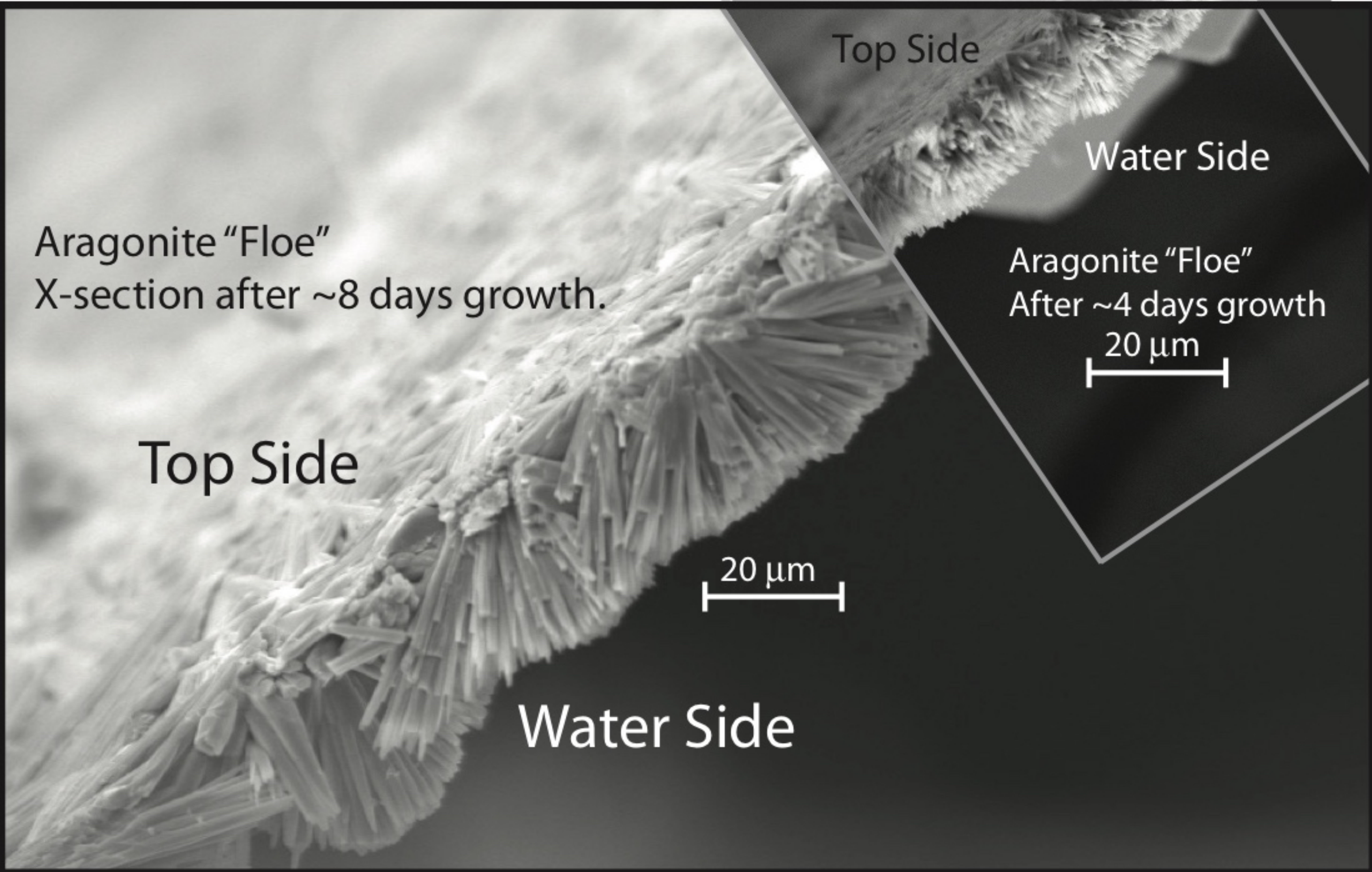
Geology Compiled from Blake et al. 1971, Preliminary Geologic Map of Western Sonoma County and Northernmost Marin County, California, USGS Open File Map

Fault features compiled by Robert Coleman, Stanford Geologic Survey, 1999.









Aragonite "Floe"
X-section after ~8 days growth.

Top Side

Water Side

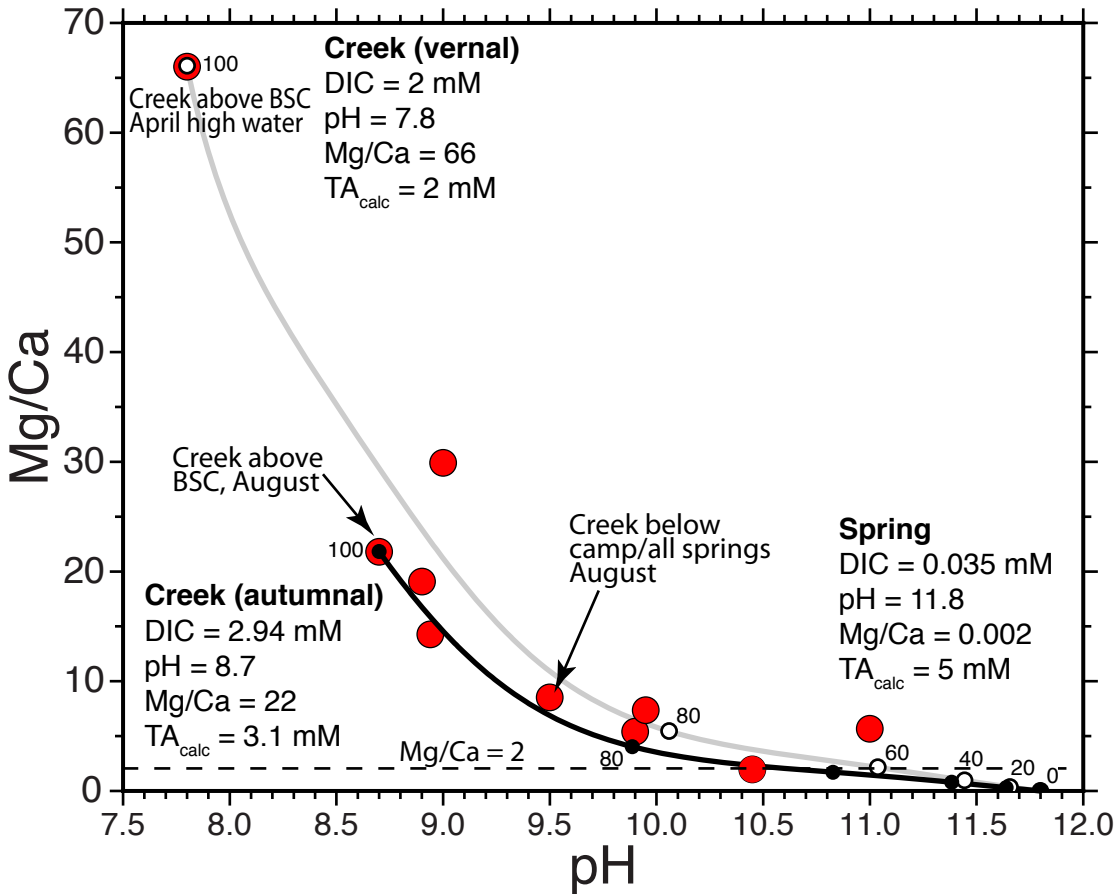
Aragonite "Floe"
After ~4 days growth

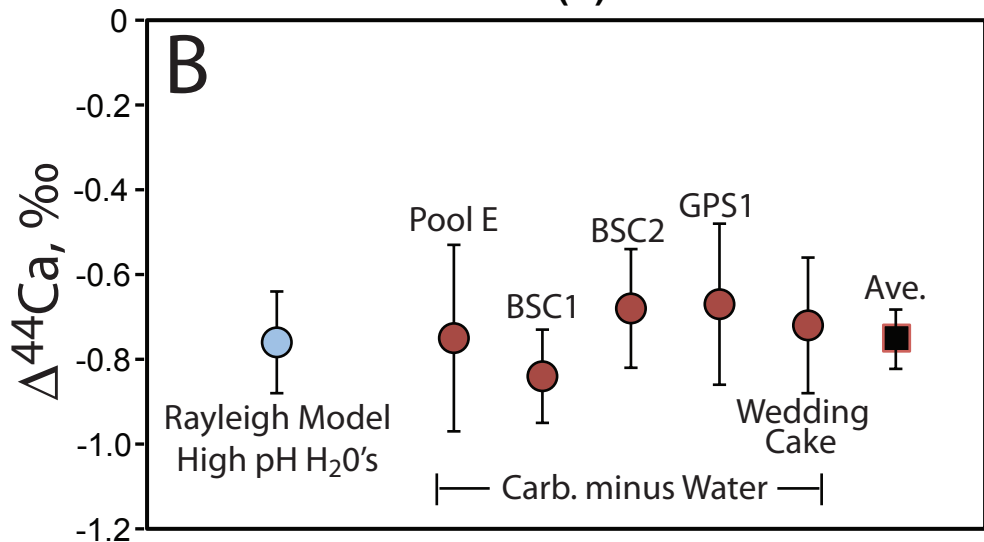
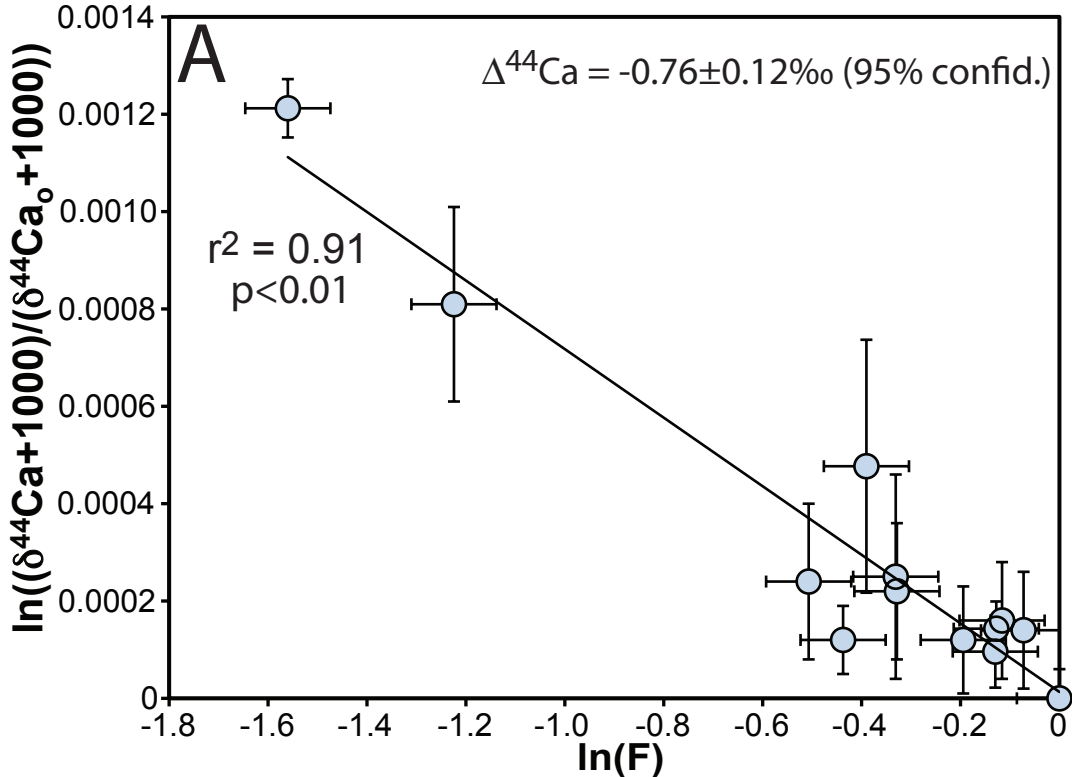
20 μm

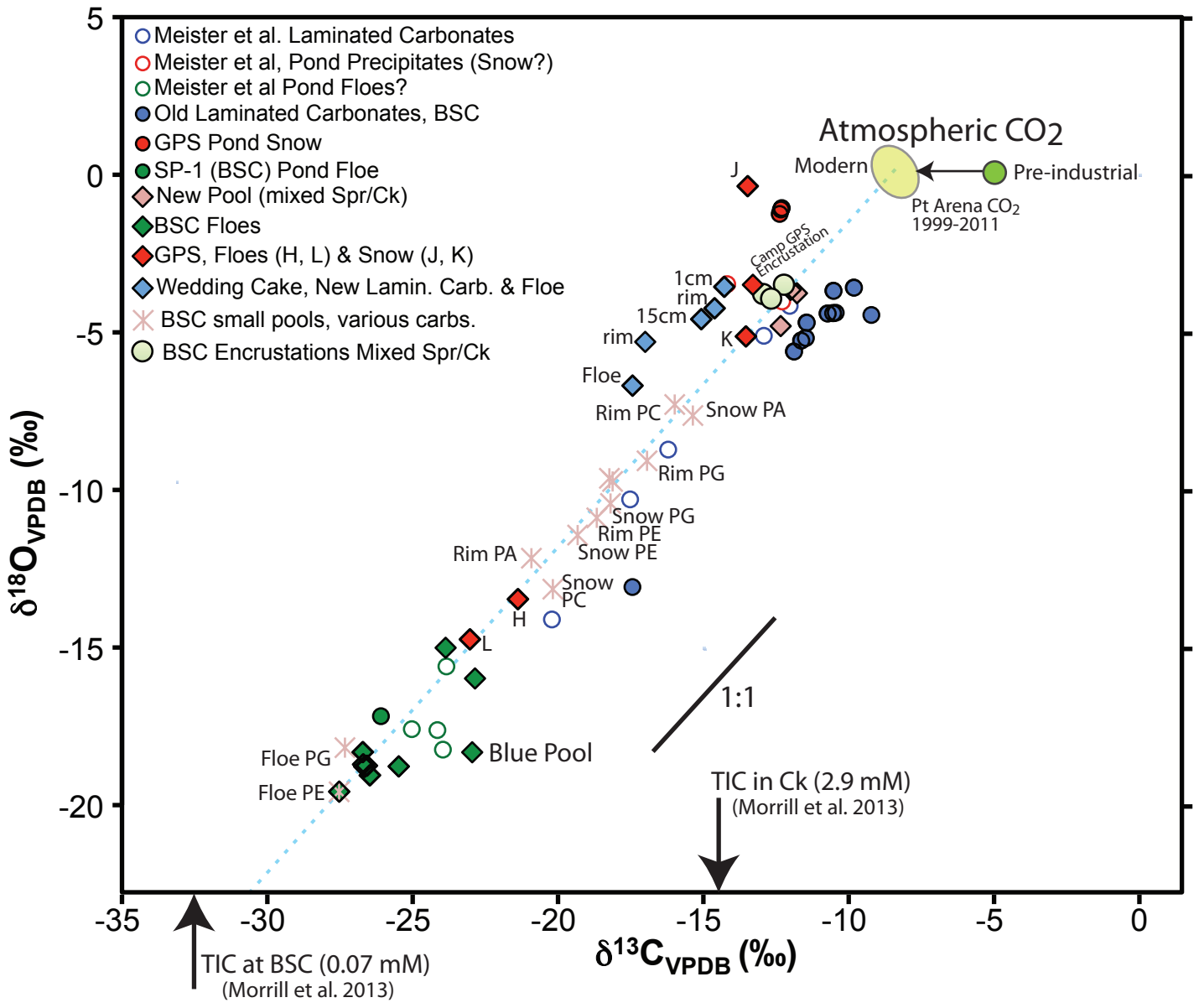
Top Side

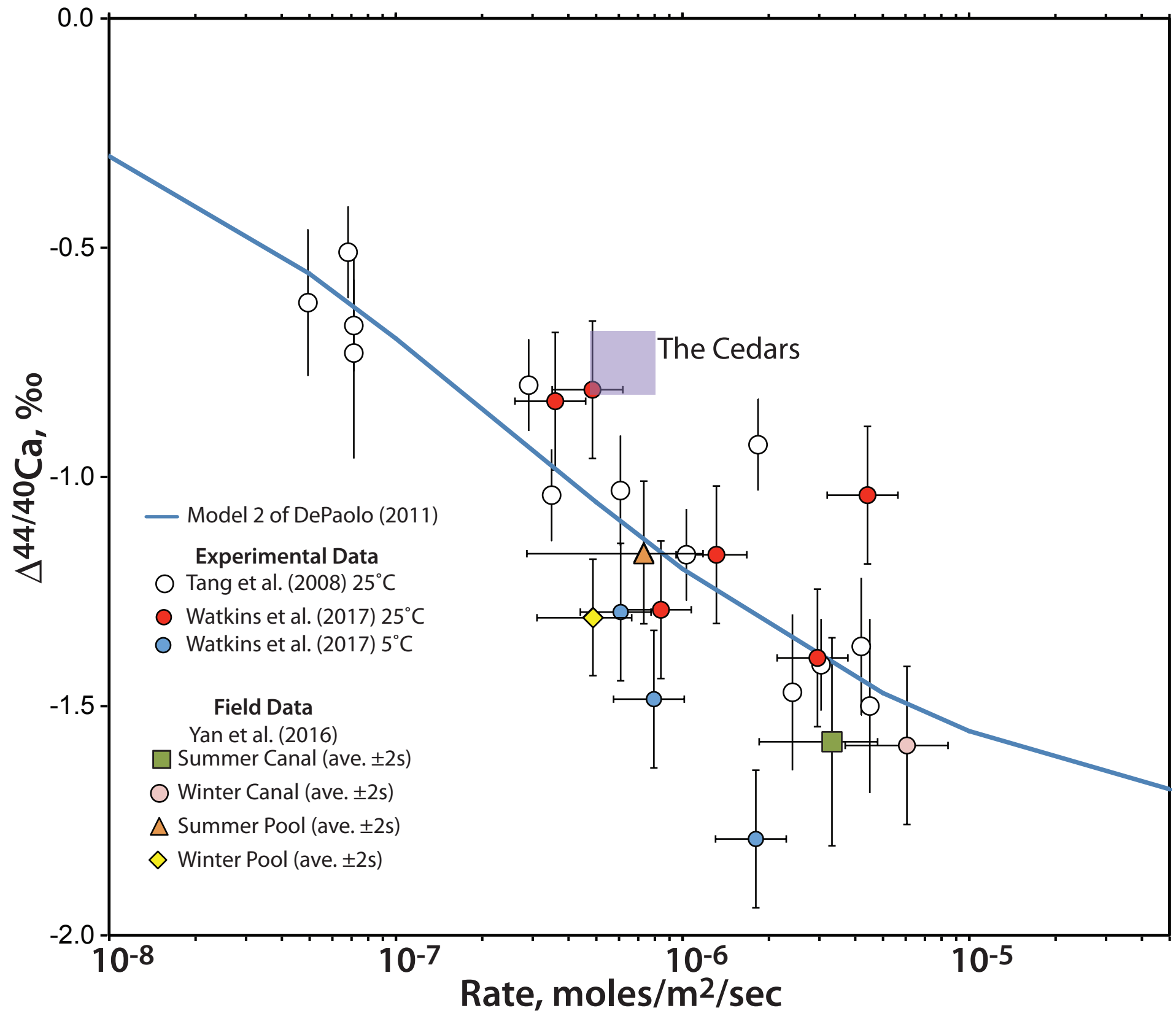
20 μm

Water Side









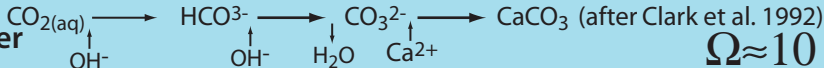
Air

Pool-Surface Crystallization of Ca-Carbonate

Atmospheric CO_2 ($\delta^{13}\text{C}_{\text{VPDB}} = -8.4$; $\delta^{18}\text{O}_{\text{VPDB}} = +0.1$)



Surface tension layer



$\Omega \approx 10$

pH=11

aragonite

calcite

100 μm

Spring
Water

$\Omega \approx 1$

pH=11.5

Mg/Ca \ll 0.01

[Ca] = 1.25 mM

[DIC] = 0.035

